JGR Solid Earth

RESEARCH ARTICLE
10.1029/2022JB026313

Special Section:
Understanding and anticipating Induced Seismicity: from mechanics to seismology

Rate and State Simulation of Two Experiments With Pore Fluid Injection Under Creep Conditions

J. W. Rudnicki[1]

[1]Department of Civil and Environmental Engineering and Department of Mechanical Engineering, Northwestern University, Evanston, IL, USA

Key Points:

- Simulations corroborate the observation that increase in pore fluid pressure can induce rapid slip in a velocity strengthening material
- Rate and state friction suggests an alternative explanation for the approach to failure than one based on the usual Coulomb condition
- Simulations demonstrate the significance of the effect of normal stress changes on the state variable

Supporting Information:

Supporting Information may be found in the online version of this article.

Correspondence to:

J. W. Rudnicki,
jwrudn@northwestern.edu

Citation:

Rudnicki, J. W. (2023). Rate and state simulation of two experiments with pore fluid injection under creep conditions. *Journal of Geophysical Research: Solid Earth*, *128*, e2022JB026313. https://doi.org/10.1029/2022JB026313

Received 22 DEC 2022
Accepted 17 APR 2023

Author Contributions:

Funding acquisition: J. W. Rudnicki

Abstract This study uses a spring-block model and rate and state friction to simulate experiments conducted in a double direct-shear apparatus on carbonate fault gouge (Scuderi et al., 2017, https://doi.org/10.1016/j.epsl.2017.08.009) and on shale bearing rock (Scuderi & Collettini, 2018, https://doi.org/10.1029/2018jb016084). Both sets of experiments used the same loading protocol and injected pore fluid under creep conditions. When velocity strengthening rate and state friction is used to simulate the experiments on the carbonate fault gouge the results agree well with the observed onset of tertiary creep in the experiment. Thus, the simulation reinforces the observation that pore fluid injection can induce rapid slip even when the friction relation is velocity strengthening. The rate and state framework provides an interpretation alternative to the standard one of the Mohr's circle moving to the left as pressure increases. In the rate and state framework, the friction coefficient must increase with pore pressure increase. The shale has a low nominal friction coefficient (0.28) and is much more velocity strengthening than the carbonate. The simulation agrees with the observations that increases in pore pressure induce an increase in slip velocity but the magnitudes reach only about 100 microns/s by the end of the experiment. The simulation for the shale also agrees well with the magnitude of the observed displacement at the end of the experiment but observed displacement is increasing much more rapidly the calculated. Although the calculations agree well with features of the observations near failure, the overall curves of displacement and velocity are significantly different.

Plain Language Summary Recent industrial processes that involve injection of fluids, such as geothermal stimulation, disposal of waste water from hydraulic fracturing and carbon sequestration, have induced seismicity that has caused concern and resulted in discontinuation of the activity. Although field experiments are ultimately necessary to establish the conditions for safe operation, laboratory experiments on fluid injection provide a more controlled environment that can yield insight into the basic physical mechanisms. Numerical simulations can test the models for such mechanisms and provide a basis for extrapolation to field conditions. This study uses a simple model and a well-established formulation of rock friction to simulate injection experiments on two types of fault zone material. For one, the simulation agrees well with the experiment and reinforces the observation that fluid injection can induce rapid slip for frictional behavior thought to suppress it. The good agreement suggests another interpretation for the failure process and allows simulation conditions not tested in the experiments. For the other material, the simulations are consistent with the observation that the pressure increases do not induce large slip velocities. Nevertheless, differences between the measured and calculated curves suggest that mechanisms other than those included in the simple model are significant.

1. Introduction

Increases in pore fluid pressure are an important mechanism to promote failure (rapid slip) on fault surfaces. The basic mechanism is well-understood in terms of the Coulomb condition. The frictional resistance is given by $\tau = \mu_0(\sigma - p)$ where μ_0 is a friction coefficient, σ is the resolved total compressive normal stress on the surface and p is the pore fluid pressure. An increase in pore pressure reduces the effective normal stress $\bar{\sigma} = \sigma - p$ and, hence, the frictional resistance. Failure is predicted to occur when the applied shear stress is equal to the resistance. A limitation of this explanation is that the criterion does not indicate the nature of the predicted slip, in particular, whether it is slow, rapid, or dynamic (seismic).

This mechanism has been corroborated by the field experiment at Rangley, Colorado (Raleigh et al., 1976) and suggested as playing a role in a variety of geological processes, for example, overthrust faulting (Hubbert &

Rubey, 1959) and reactivation of misoriented weak faults (Byerlee, 1990; Collettini & Sibson, 2001; Faulkner & Rutter, 2001; Yeck et al., 2016). There are many recent examples of increases of pore fluid pressure by injection of fluids into the subsurface for technological processes that have induced earthquakes. These processes include enhanced geothermal stimulation (Barbour et al., 2017; Bourouis & Bernard, 2007; Charéty et al., 2007; Deichmann & Giardini, 2009; Lengliné et al., 2017; Majer et al., 2007; Martinez-Garzón et al., 2014), disposal of waste fluids from hydraulic fracturing (Ake et al., 2005; Frohlich, 2012; Frohlich et al., 2014; Healy et al., 1968; Holland, 2011; Horton, 2012; Hsieh & Bredehoeft, 1981; Keranen et al., 2013; Kim, 2013; Raleigh et al., 1976; Rubinstein et al., 2012; Zoback & Harjes, 1997) and injection of CO_2 for sequestration (Evans et al., 2012). A particularly dramatic example is the rapid increase in seismic events in the mid-continental United States (Ellsworth, 2013). In addition, in a field experiment Guglielmi et al. (2015) observed creeping slip induced by fluid injection.

Although the Coulomb condition continues to be useful for determining the onset of slip, extensive experimental observations (Marone, 1998) have shown that rock friction is well-described by the rate and state formulation (Dieterich, 1979; Ruina, 1983), at least at slow sliding velocities. Use of rate and state friction in simulations of earthquakes has produced results consistent with many observations and, more generally, has contributed to the understanding of earthquakes, including initiation and arrest and slow earthquakes (e.g., Ampuero & Rubin, 2008; Dieterich, 1986; Dieterich, 1992; Lapusta et al., 2000; Liu & Rice, 2005, 2007). A number of analyses and simulations have used rate and state friction to examine the effects of fluid injection on slip (Almakari et al., 2019; Andrés et al., 2019; Cueto-Felgueroso et al., 2017, 2018; Dublanchet, 2019; Heimisson et al., 2021, 2022; Larochelle et al., 2021; McClure & Horne, 2011; Yang & Dunham, 2021). In addition, Garagash and Germanovich (2012) have used slip-weakening friction which, in some circumstances, can be considered an approximation to rate and state friction (Garagash, 2021), to examine the effects of fluid injection on slip.

Although field observations are the ultimate test of the effects of pore fluid on failure, their interpretation is complicated by heterogeneity of hydrologic and mechanical structure, and pumping and loading history. In particular circumstances, well-designed field tests can overcome some of these limitations. Examples are the injection tests of Raleigh et al. (1976) and Guglielmi et al. (2015). Laboratory experiments, despite their limited size and time scales, provide a more controlled environment that can yield an understanding of fundamental processes. Simple models that simulate the experiments can assess whether the mechanisms included in the models are sufficient to describe well the response or more complex formulations are needed. In addition, simulations can extend results for parameter values and loading programs beyond those achievable in experiments and aid in extrapolation to field applications. A number of recent experiments have examined the effects of pore fluid injection on slip. These include Cappa et al. (2019), French et al. (2016), Gori et al. (2021), Noël, Passelégue, et al. (2019), Passelégue et al. (2018), Scuderi et al. (2017), Scuderi and Collettini (2018) and Wang, Kwiatek, Rybacki, Bonnelye, et al. (2020); Wang, Kwiatek, Rybacki, Bohnhoff, and Dresen (2020).

This study focuses on the experiments of Scuderi et al. (2017) on carbonate bearing fault gouge and of Scuderi and Collettini (2018) on a shale bearing rock. Both conducted creep experiments using a double direct shear apparatus and the same loading program: (a) advance the vertical ram at 10 μm/s for 13 mm; (b) stop the vertical ram for 30 min; (c) change the stress to 80% or 90% of the steady state level; (d) creep for 60 min; (e) while continuing to creep, increase the pore pressure stepwise at two rates 1 MPa/hr and 0.2 MPa/12 min. For the carbonate gouge, Scuderi et al. (2017) observe that the variation of slip velocity is typical of creep behavior (Brantut et al., 2013). More specifically, the slip velocity initially decreases (primary creep), then is roughly constant (secondary creep). Finally, the slip accelerates and the slip rate becomes essentially vertical on a graph of slip versus time (tertiary creep). Scuderi et al. (2017) identify the departure of the slip from the linear trend of secondary creep as the onset of tertiary creep. For the shale Scuderi and Collettini (2018) find that the slip does not follow the typical creep pattern observed for the carbonate gouge. Slip and slip velocity do accelerate toward the end of the experiment but the slip velocity never gets very large.

I simulate these experiments using a simple spring - block model (Figure 1) and rate and state friction. The spring - block model is too simple to describe slip on surfaces in a continuum but it is a good approximation for an experiment in which slip occurs roughly simultaneously on the frictional surface within the resolution of the experiments. The model is not appropriate for experiments in which heterogeneous slip on the surface is monitored. Two experimental studies of fluid injection just cited are of this type (Gori et al., 2021; Passelégue et al., 2018).

Passelégue et al. (2018) conduct an axisymmetric compression test in which they inject fluid through a bore hole directly to a saw cut in Westerly granite. They use elastic wave velocity measurements to track the progression of

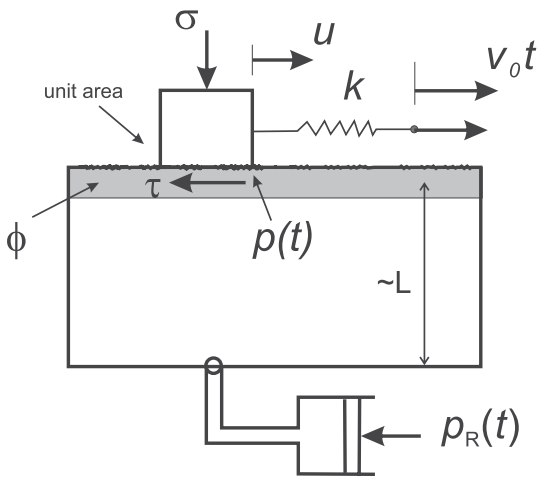

Figure 1. Spring block model.

fluid pressure along the fault. They find that for low injection rates, the pore pressure is relatively uniform along the fault and standard application of the effective stress principle and Coulomb criterion adequately predicts the onset of rapid slip. However, for fast injection, they find that the pore pressure distribution on the fault is heterogeneous and slip is initiated in a local region where the pore pressure is sufficiently high.

Gori et al. (2021) inject fluid into an interface in a quadrilateral specimen of PMMA. The distribution of pore pressure on the interface is measured by pressure sensitive tape. Strain and slip are measured by a strain-gage near the interface and strains by digital image correlation and ultrahigh-speed photography. They find that rapid injection initiates dynamic ruptures at lower pressure and smaller nucleation lengths than predicted for quasi-static loading. In contrast, slow injection causes a gradual nucleation process with fluid spreading along the interface and a slow acceleration of slip.

The goal of this study is to determine to what extent the observed behavior can be explained by rate and state friction. I show that simulation of the experiment of Scuderi et al. (2017) agrees well with the observations. In particular, the calculated time at which rapid slip occurs agrees well with the observed onset of tertiary creep. In the simulations, failure is identified with the onset of rapid slip and there is no need to impose an external failure criterion, such as the Coulomb criterion. Calculations are also done for other loading programs not considered in the experiments, that is, linear, ramp and periodic. The calculations for the shale experiments (Scuderi & Collettini, 2018) are consistent with the observations that pore fluid pressure increase does cause the slip velocity to increase. But the strong velocity strengthening of the shale prevents the slip velocity from getting very large. In addition, the calculations for the shale agree well with the observed displacements at the end of the experiment. However, for both materials, differences between the observed and calculation velocity and displacement curves suggest that other factors not modeled by rate and state friction are important.

2. Model Formulation

The experiment is simulated by a block spring system shown in Figure 1 (Segall & Rice, 1995). The block has a unit area and rests on a thin layer of gouge with pore pressure p and porosity ϕ. A pore fluid reservoir with pressure p_R is located at a distance $\sim L$ from the block. Displacement of the right end of the spring is imposed at a constant rate v_0 and slip of the block is u. The spring has a stiffness k and the constant normal force is σ. Motion of the block is resisted by a frictional force τ. Thus, the equation of motion of the block is

$$k(v_0 t - u) - \tau = \omega v \tag{1}$$

where $v = du/dt$. The term on the right side is the radiation damping approximation to inertia (Rice, 1993; Rice & Tse, 1986) and $\omega = G/2v_s$ where G is the shear modulus and v_s is the shear wave speed. This term is very small, but prevents the velocity from becoming unbounded when the quasistatic solution is unstable.

The frictional stress is given by the rate and state form (Dieterich, 1979, 1980; Ruina, 1981, 1983)

$$\tau = (\sigma - p)\left[\mu_0 + a\ln(v/v_R) + b\ln(\theta/\theta_R)\right] \tag{2}$$

where p is the pore fluid pressure, a and b are constitutive parameters, θ is the state variable, v_R and θ_R are reference values, and μ_0 is the steady state coefficient of friction when v and θ are equal to their reference values. Two forms are typically used for the rate of change of the state variable: The aging or slowness law

$$\frac{d\theta}{dt} = 1 - \frac{\theta v}{d_c} \tag{3}$$

and the slip law

$$\frac{d\theta}{dt} = -\frac{\theta v}{d_c}\ln\left(\frac{\theta v}{d_c}\right) \tag{4}$$

where d_c is a characteristic decay distance. Both laws linearize to the identical form. The primary difference between them is their behavior for very slow velocity. At zero velocity the state increases linearly with time for the aging law but does not change for the slip law. For steady state sliding, $d\theta/dt = 0$ and both laws give $\theta_{ss} = d_c/v_{ss}$. If $\theta_R = d_c/v_R$. Then the steady state stress is

$$\tau_{ss} = (\sigma - p)\left[\mu_0 + (a-b)\ln(v_{ss}/v_R)\right] \tag{5}$$

For $a > b$, the steady state stress increases for an increase in velocity. In this case, the response is said to be velocity strengthening and small perturbations from steady state sliding always decay. For $b > a$ the response is velocity weakening and small perturbations from steady sliding can increase in time if the spring stiffness k is sufficiently low. More specifically, for drained conditions (constant pore pressure p), k must be less than a critical value (Ruina, 1981, 1983)

$$k_{crit} = (\sigma - p)(b-a)/d_c \tag{6}$$

For Coulomb friction, the frictional resistance is proportional to the effective compressive stress, $(\sigma - p)$. Consequently, an increase in pore pressure decreases the frictional resistance and, thus, is destabilizing. However, as Scuderi et al. (2017) note, an increase in pore pressure decreases k_{crit} and, hence, is stabilizing.

Recent experiments Bhattacharya et al. (2022) have indicated that the slip law describes data better than the aging law even at very low sliding velocities (3μm/s to less than 10^{-5} μm/s). Nevertheless, I have used the aging law. A few simulations indicate some differences, but they were significantly smaller than the differences between the data and the simulations.

Experiments have indicated that a change in effective normal stress can change the state (Linker & Dieterich, 1992; Richardson & Marone, 1999) and Linker and Dieterich (1992) proposed that the change is described by

$$\frac{\alpha}{b}\frac{\theta}{\bar{\sigma}}\frac{d\bar{\sigma}}{dt} \tag{7}$$

where $\bar{\sigma} = \sigma - p$ is the effective normal stress and α is another parameter. On theoretical grounds (Perfettini et al., 2001; Rice et al., 2001) $0 \le \alpha \le \mu_0$ and measurements (Linker & Dieterich, 1992; Richardson & Marone, 1999) have shown that for rocks sliding at velocities of order 1–10 μms α is 1/3 to 1/2 of μ_0. This term Equation 7 should be subtracted from the right sides of Equations 3 and 4. A recent study of normal stress effects using improved experimental techniques (Kilgore et al., 2017) has indicated that there needs to be some revision of Equation 7. This issue is discussed further later in the study.

Effects of diffusion are included by adding two equations following Segall and Rice (1995). Based on the experiments of Marone et al. (1990) for shearing of quartz gouge, they proposed the following equation for the change of porosity ϕ:

$$\dot{\phi} = -\frac{v}{d_c}(\phi - \phi_0 - \epsilon \ln(v/v_R)) \tag{8}$$

where ϕ_0 is the initial porosity and ϵ is a parameter. Segall and Rice (1995) briefly comment on a different form for the porosity change that they attribute to Sleep (1995). In this form the porosity depends on the logarithm of the state variable, rather than the velocity, as in Equation 8. Segall and Rice (1995) note that both have the same steady state and linearization about steady state. Predictions are similar for velocity stepping and slide-hold slide tests but differ significantly for steps in normal stress at constant sliding velocity (Rudnicki, 2022). Because the Segall and Rice (1995) form does not depend on the state it predicts no change of porosity; the Sleep (1995) form does because the Linker and Dieterich (1992) effect causes changes in state due to changes in normal stress. A spring-block simulation (Rudnicki, 2022) suggests other differences between the formulations that could be important, but the Segall and Rice (1995) form is used here.

The second equation describes diffusion of pore fluid between the reservoir and the fault surface. Rather than using the diffusion equation, Segall and Rice (1995), for reasons of simplicity, used the approximation of Rudnicki and Chen (1988): the fluid mass flux is assumed to be proportional to the difference between the pore pressure in the reservoir p_R and on the slip surface p rather than satisfying Darcy's law. The result is

$$c^*(p_R - p) = \dot{p} + \dot{\phi}/\beta \tag{9}$$

where the elastic part of the porosity has been neglected, c^* is the reciprocal of a diffusion time and $\beta = \phi_0(\beta_f + \beta_\phi)$, β_f is the compressibility of the pore fluid and β_ϕ is the compressibility of the pore space (See Chambon & Rudnicki, 2001 for a discussion of including the poroelastic term).

On physical grounds it is preferable to write the equations in terms of non-dimensional variables; for example, it is better to measure the time in terms of the time scale of rate and state processes, d_c/v_R than minutes or seconds. The nondimensional quantities are $V = v/v_R$, $T = v_R t/d_c$, $U = u/d_c$, $\Sigma = \tau/\bar{\sigma}_0$ where $\bar{\sigma}_0$ is the (constant) initial value of the effective stress, $P = \Delta p/\bar{\sigma}_0$, where Δp is the change in pore pressure from its initial value, $K = kd_c/\bar{\sigma}_0 A$ (A is the cross-sectional area of the block, equal to 1 in Equation 1) and $\Omega = \omega v_R/\bar{\sigma}_0$. Equation 9 then becomes

$$\hat{c}(P_R - P) = \dot{P} + \dot{\Phi}/\hat{\beta} \tag{10}$$

where $\hat{c} = c^* d_c/v_R$, $P = \Delta p/\bar{\sigma}_0$, $\Phi = \phi - \phi_0$ and $\hat{\beta} = \sigma_0\beta$

Differentiating Equations 1 and 2, eliminating $d\Sigma/dT$, and solving for dV/dT gives

$$\dot{V} = \frac{K\left[(v_0/v_R) - V\right] - (1-P)(b/\Theta)\dot{\Theta} + \dot{P}\mu(V,\Theta)}{(1-P)(a/V) + \Omega} \tag{11}$$

where the superposed dot indicates $d(\ldots)/dT$ and $\mu(V,\Theta)$ is the friction coefficient in square brackets in Equation 2. Writing Equation 3 in non-dimensional form and including the term Equation 7 gives

$$\dot{\Theta} = 1 - V\theta + \frac{\alpha}{b}\frac{\theta}{(1-P)}\dot{P} \tag{12}$$

When $P_R(T)$ is specified Equations 10–12 are three ordinary differential equations for V, P, and Θ. The displacement U can be determined by integrating V and then Σ can be determined from Equations 2 or 1. Alternatively, the system can be written as five equations for V, Θ, P, U and Σ. However, not all of the equations are needed during the different loading segments.

Before fluid injection begins in the experiment, the pore pressure is its constant initial value which is included in $\bar{\sigma}_0$. Hence, P and $\dot{P}$ are zero in Equations 11 and 12. Scuderi et al. (2017) and Scuderi and Collettini (2018) begin their experiments by advancing the ram at 10 μm/s for 13 mm to establish a steady state. Therefore, I take $v_R = 10$ μm/s. Since the load point velocity v_0 represents ram velocity, $V = 1$, $\Theta = 1$, $\Sigma = \mu_0$ and $U = T$ during this segment.

Next Scuderi et al. (2017) stop the ram for 30 min. This corresponds to taking $v_0 = 0$ in Equation 11. The pore pressure is still zero. Thus, only Equations 11 and 12 (with $\dot{P} = 0$) need to be solved. This is the only segment in which the stiffness K plays a role.

After the zero load point segment, the shear stress is changed from its value to either 80% or 90% of the steady state value $\bar{\sigma}_0\mu_0$. I assume that change occurs suddenly and therefore the state remains the same as its last value from the zero load point segment. The sudden change in stress causes a sudden change of velocity. Solving Equation 2 for the velocity at constant state yields

$$V_+ = V_-\exp\{(\xi\mu_0 - \Sigma_-)/a\} \tag{13}$$

where the subscript "−" refers to the value at the end of the zero load point segment, "+" refers to the beginning of the creep segment, and ξ is 0.8 or 0.9.

Thereafter, the stress is held constant and the specimen creeps for an additional 60 min before fluid injection begins. During this segment, Equations 11 (with $K = 0$) and 12 need to be solved. Once fluid injection begins, the pore pressure in the reservoir is increased in steps of 1 MPa/hr or 0.2 MPa/12 min.

For the shale (Scuderi & Collettini, 2018) the response is determined by solving Equations 10, 11 (with $K = 0$) and 12. For the carbonate gouge, the permeability is large, $\sim 10^{-17}$ m^2 and, as shown in Figure 6 of Scuderi et al. (2017), the pore pressure quickly equilibrates between the up-stream and down-stream reservoirs. Consequently, conditions are fully drained and the pore pressure in the gouge layer can be taken as equal to that in the reservoir, $P = P_R$. Equation 10 is not needed and, except for the steps, the pore pressure is constant. Therefore,

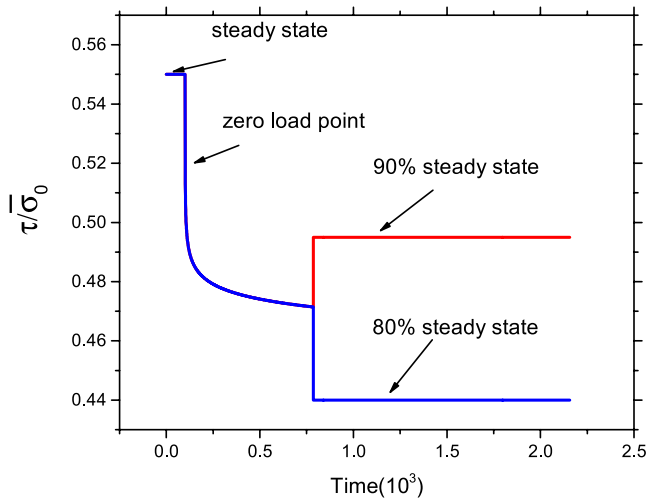

Figure 2. Simulation of loading program.

$\dot{P} = 0$ in Equations 11 and 12. However, the jump in effective stress (due to the jump in pore pressure) causes a jump in state given by (Linker & Dieterich, 1992)

$$\Theta_+ = \Theta_- \left(\frac{\bar{\sigma}_-}{\bar{\sigma}_+} \right)^{\alpha/b} \tag{14}$$

where again the "−" denotes the value just before the jump and the "+" the value just after. For creep conditions, this jump in state is accompanied by a jump in velocity. Evaluating Equation 5 for τ_+ and τ_-, equating them, and using Equation 14 yields

$$V_+ = V_- \left(\frac{\bar{\sigma}_+}{\bar{\sigma}_-} \right)^{\frac{\alpha}{a}} \exp\left[\frac{-\Delta\bar{\sigma}}{a\bar{\sigma}_+} \mu(V_-, \Theta_-) \right] \tag{15}$$

where $\Delta\bar{\sigma} = \bar{\sigma}_+ - \bar{\sigma}_-$, the difference between effective normal stress just after and just before the jump. The procedure is to solve Equations 11 and 12 with $\dot{P} = 0$ between the jumps and to use the jump conditions Equations 14 and 15 to get the initial conditions for the next jump.

3. Carbonate Gouge

3.1. Parameters

Most of the parameters can be taken from Scuderi et al. (2017). They initially advance the ram at 10 μm/s for 13 mm to establish a steady state. Therefore, I take $v_R = 10$ μm/s. The cross-sectional area of the frictional surface is $A = 5.54$ cm × 5.55 cm = 30.7 cm^2, the stiffness of the vertical ram is 386.12 kN mm and the steady state value of the friction coefficient $\mu_0 = 0.55$. There is a misprint in the stated values of the normal stress, confining pressure, and initial pore fluid pressure in Scuderi et al. (2017) but the correct values (Scuderi, personal communication, 2022) are 5 MPa, 28 and 13 MPa, respectively. This gives a total normal stress of 33 MPa (5 MPa + 28 MPa) and an initial effective stress of $\bar{\sigma}_0 = 20$ MPa. Scuderi et al. (2017) do not give values of the rate and state parameters a, b and d_c but Figure 4 of Scuderi and Collettini (2016) gives values for $a - b$ and d_c for carbonate gouges at different sliding velocities and effective compressive stresses. Values were obtained for velocity jumps of 0.1–1 μm/s, 1–10 μm/s and 10–100 μm/s and effective pressures of 3, 7, 10, 18, and 30 MPa. They found that the rate and state parameters varied with both sliding velocity and pore fluid pressure. Scuderi and Collettini (2016) do not give separate values for a and b but Scuderi (personal communication, 2022) provided the data set in tabular form. Because the initial effective stress in Scuderi et al. (2017) is $\bar{\sigma}_0 = 20$ MPa and the initial sliding velocity is 10 μm/s, I considered the values of a, b, and d_c at the effective confining stress of 18 MPa for the two larger velocity jumps. There were eight of these but 6 were better fit by a two state variable description. I averaged the remaining two to get $a = 0.0143$, $b = 0.0100$ and $d_c = 0.0263$ mm. This gives $a-b = 0.0043$ corresponding to slightly velocity strengthening behavior. For these values $t = 1$ hr corresponds to $T = 1{,}371$ and $K = kd_c/\bar{\sigma}_0 A = 0.165$. A value of α is also not given but it must be between zero and μ_0 and I take $\alpha = 0.3$. A pore pressure step of 1 MPa corresponds to $P = 0.05$ and, therefore, the step of 0.2 MPa corresponds to 0.01. The parameters are summarized in Table S1 (Supporting Information S1).

3.2. Results

Figure 2 shows the simulation of the stress in the loading program used by Scuderi et al. (2017). It starts at the end of the steady state period when $\tau/\bar{\sigma}_0 = \mu_0$. (Only a portion $T = 100$ is shown). The 30 min ($T = 1{,}371/2 = 685.5$) during which the ram is stopped is simulated by setting the load point velocity $v_0 = 0$ in Equation 1. This causes a relaxation of the shear stress as shown. At the end of this period the shear stress is suddenly changed to 80% or 90% of the steady state level and remains there until the end of the experiment. Figure 3 of Scuderi et al. (2017) shows the stress increasing to the 80% or 90% level from the end of the period during which the ram is stopped, but the simulation shows a decrease to the 80% level. Then the sample is allowed to creep for 60 min ($\Delta T = 1{,}371$) and fluid injection begins at $T = 2156.5$ (including the steady state segment).

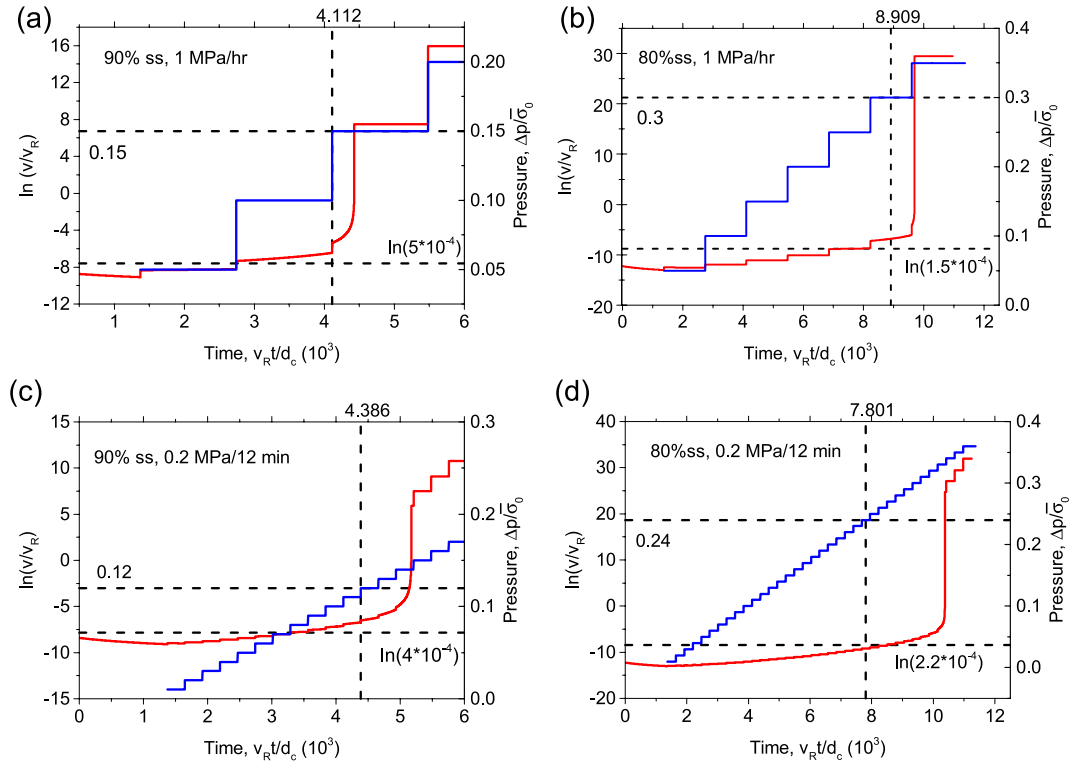

Figure 3. Results for the four cases. First column (a, c) shows 90% of steady state and the second (b, d) 80%. First row (a, b) shows the pore pressure rate of 1 MPa/1 hr and the second (c, d) 0.2 MPa/12 min. The red trace shows the logarithm of the velocity of the block divided by the reference velocity against (non-dimensional) time and the blue the pore pressure increase (right axis). The lower horizontal line is the steady state velocity during secondary creep identified by Scuderi et al. (2017). The pore pressure and the time at the onset of tertiary creep identified by Scuderi et al. (2017) are the upper horizontal line and the vertical line, respectively.

Figure 3 plots ln (v/v_R) (red trace and left axis) and the non-dimensional pore pressure change $P = \Delta p/\bar{\sigma}_0$ (blue trace and right axis) against the non-dimensional time $T = v_R t/d_c$ for the four cases: 80% or 90% of the steady state shear stress and pore pressure rates of 1 MPa/hr and 0.2 MPa/12 min. Time is measured from the beginning of the creep state. (For the case of 90% of steady state and a rate of 0.2 MPa/12 min, there seems to be a small discrepancy between the time and pore pressure at the onset of tertiary creep reported by Scuderi et al. (2017). The time at which the pore pressure would be 16.2 MPa is significantly (52 min) later than the 200 min reported and shown in their Figure 4a, for the onset of tertiary creep. The discrepancy was eliminated by using a pore pressure of 15.4 MPa and a time to onset of tertiary creep of 192 min.) As expected, rapid increases in velocity occur close to the steps in pore pressure. The lower horizontal line on each graph is the logarithm of the velocity (divided by the reference velocity) for the linear increase of slip during secondary creep shown in Figure 4 of Scuderi et al. (2017). The velocity in the simulation is not constant but it is similar in magnitude. Because the velocity is several orders of magnitude less than the reference velocity, and the difference between the simulation and a constant velocity is small, distinguishing them would be difficult. The vertical line marks the onset of tertiary creep identified by Scuderi et al. (2017) and the upper horizontal line the pore pressure at which it occurred. In the simulation the nearly vertical segment at which the velocity increases from several orders of magnitude below the reference value to several orders of magnitude above is considered to be the occurrence of tertiary creep. Because the onset of rapid velocity is easier to identify in the simulation, as expected, it occurs after the onset of tertiary creep identified in the experiment. For the 90% of steady state case, the onset precedes the full development by 13.9 min for the 1 MPa/hr rate and 36 min for the 0.2 MPa/12 min rate. For 80% of steady state, the corresponding times are 34.3 and 144.4 min. The simulation result agrees reasonably well with velocity determined from the experiment.

Figure 4 shows the observed displacement (digitized from Figures 4 and 5 from Scuderi et al., 2017) (blue) and the calculated displacement (red) against time. The vertical line indicates the time when the calculated

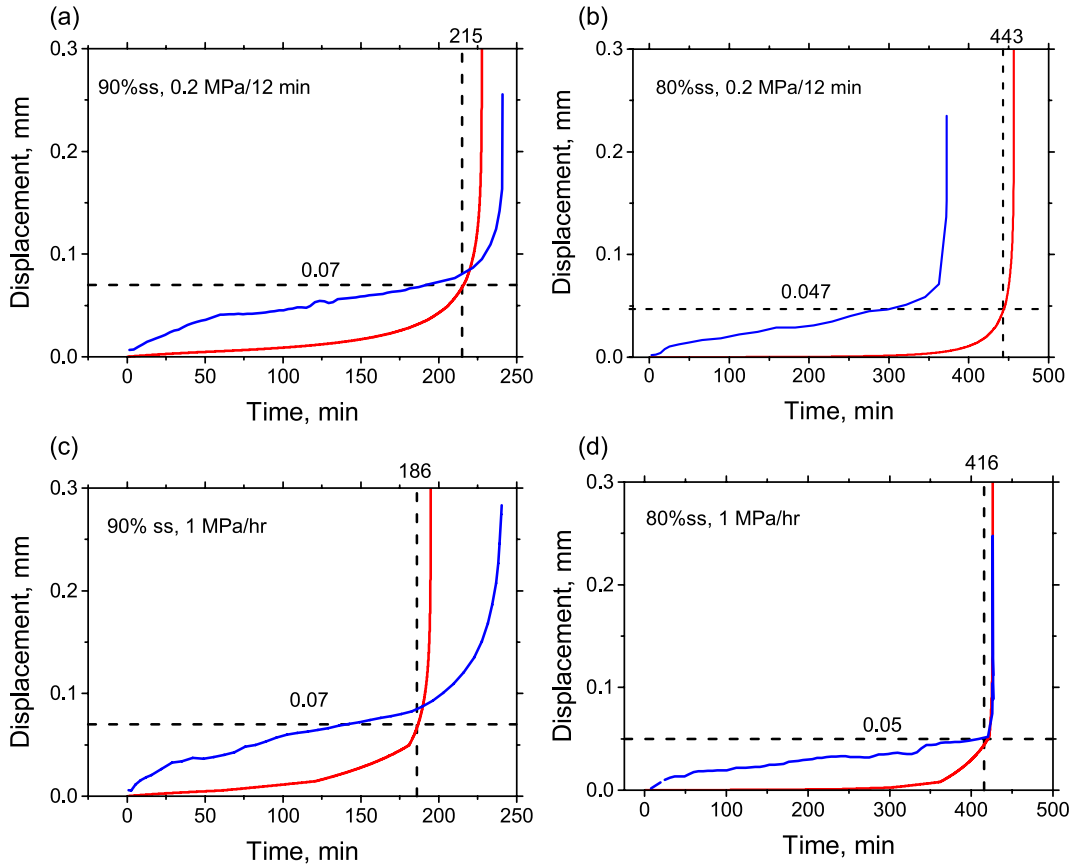

Figure 4. Plot of the measured (blue) and simulated (red) displacement against time. The vertical line indicates when the calculated displacement (marked by the horizontal line) equals that reported Scuderi et al. (2017) for the onset of tertiary creep.

displacement (marked by the horizontal line) equals that reported by Scuderi et al. (2017) for the onset of tertiary creep. As expected, this time exceeds that at which this value of displacement occurs on the measured curve. Although the agreement between calculated and observed curves is not very good overall, the agreement between the predictions of the onset of tertiary creep is good (except for Figure 4b). As noted earlier, the observed onset is expected to precede that in the calculations. That is the case, but the predictions are nearly equal in Figure 4d.

Figure 5 shows the results for the four cases, two levels of shear stress and two rates of pressure increase. As in the experiment, instability for the 1 MPa/hr rate precedes that for the 0.2 MPa/12 min rate. From the simulation results the amount is about the same for both the 80% (30.1 min) and the 90% (34.1 min) levels. Also, as in the experiment, instability for the 90% level precedes that for the 80% level. Again, the amount is about the same for the 1 MPa/hr rate (230.4 min) and the 0.2 MPa/12 min rate (226.4 min).

Scuderi et al. (2017) interpret their results in terms of the classical theory of failure sketched in Figure 6a. Because the shear stress is held constant during creep conditions, the radius of the Mohr's circle is constant and the circle moves to the left as the pore pressure increases. Failure is predicted to occur when the Mohr's circle touches the failure line. Scuderi et al. (2017) established the failure line in a separate set of experiments.

In the context of rate and state friction, the interpretation is, however, different, as sketched in Figure 6b. In rate and state friction, the surface is always sliding and, consequently, Equation 2 must be satisfied. Because shear stress is constant, the right side of the equation must also be constant. The increase of pore pressure (with fixed total normal stress) causes the first term on the right side, the effective stress σ, to decrease. Consequently, the second term on the right side, the friction coefficient, must be increasing. This is shown in Figure 7 for the 90% level with 1 MPa/hr rate. The friction coefficient suddenly increases when the jump in pore pressure causes the effective stress to suddenly decrease. In between the pore pressure jumps the effective stress is constant and so is the friction coefficient. To maintain the friction coefficient constant, the changes due to evolution of the state and the velocity must

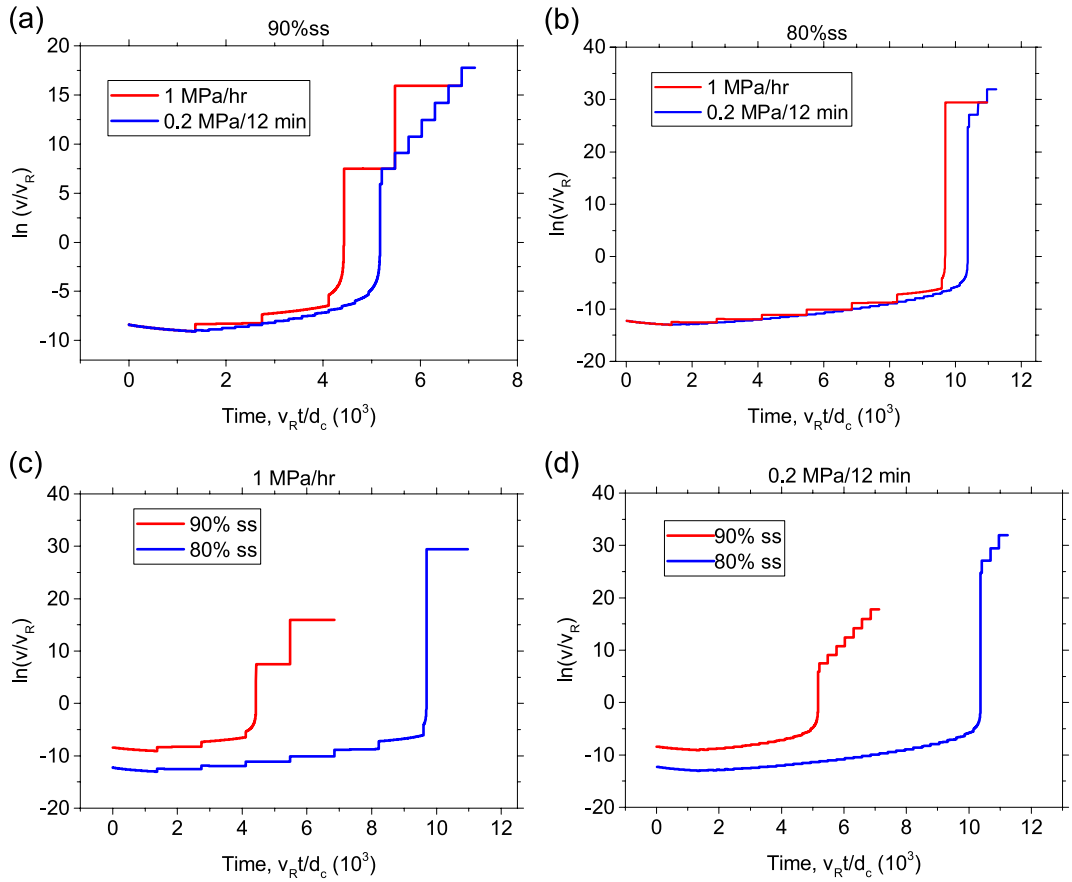

Figure 5. Compares simulation results for the four cases: 80% and 90% of steady state and 1 MPa/hour and 0.2 MPa/12 min. Each panel plots the logarithm of the non-dimensional velocity against the non-dimensional time.

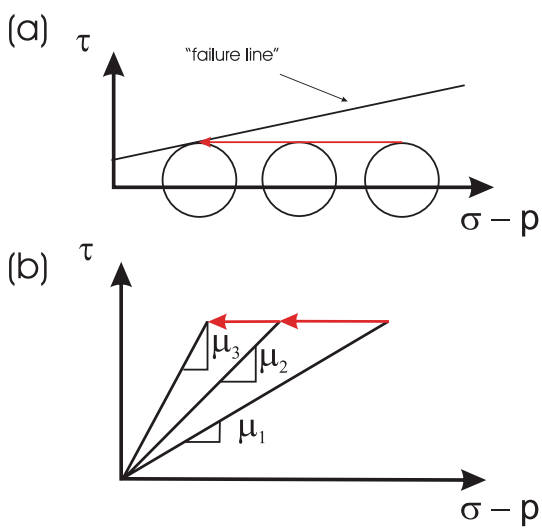

Figure 6. (a) Sketch of the classical interpretation of the failure process in the shear stress τ versus effective normal stress $\bar{\sigma} = \sigma - p$ plane. As the pore pressure increases with constant shear stress the Mohr's circle moves to the left. Failure is predicted to occur when the circle touches the failure line. (b) Sketch of the rate and state failure process. The coefficient of friction increases as the stress point moves to the left. Failure occurs with the sudden onset of rapid slip (several orders of magnitude greater than the reference velocity).

compensate. Figure 7a plots the logarithm of the state and of the velocity against non-dimensional time. The state and the velocity both begin at one, $\Theta = 1$ and $V = 1$, during the steady state portion of the test (not shown in the figure). However, during the zero load point segment of the experimental protocol (also not shown in the figure), the velocity decreases and the state increases. When the stress is jumped to 80% or 90% of the steady state value, the velocity undergoes an additional reduction according to Equation 13. Because the jump is sudden, the state does not change value. As shown in Figure 7a, the state remains large and the velocity small during the creep loading before injection and during the initial stages of injection. Small changes occur at the pore pressure jumps, but when the velocity undergoes a large increase, the state undergoes a large decrease to balance the increase in the friction coefficient with the decrease of effective compressive stress. Figure 6b sketches the rate and state failure process in the shear stress τ versus effective normal stress $\bar{\sigma} = \sigma - p$ plane. The friction coefficient simply increases until large velocity occurs. With rate and state friction, the failure criterion is built-in; there is no need to impose it from without.

Figure 8 examines the importance of the Linker and Dieterich (1992) effect due to including Equation 7. The logarithm of the velocity is plotted against non-dimensional time for each of the four cases. For each case, results of simulations in Figure 3, including the Linker and Dieterich (1992) term with $\alpha = 0.3$ are compared with simulations neglecting this effect ($\alpha = 0.0$). Also shown are curves for $\alpha = 0.4$. When $\alpha = 0$, there is no change in the state due to a change in effective stress as indicated by Equation 14. Nevertheless, even in this case the

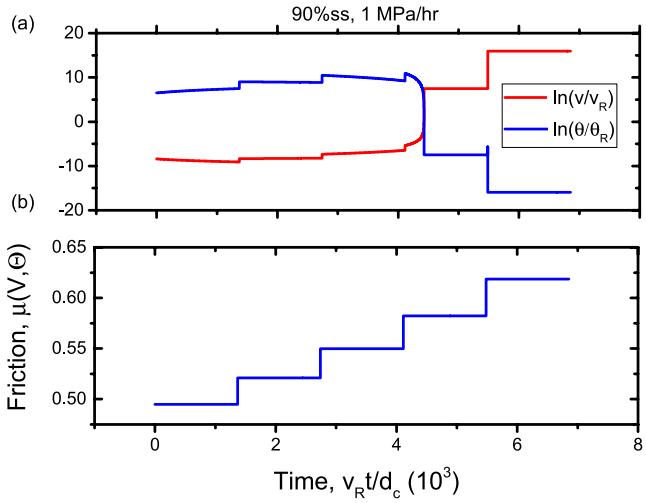

Figure 7. (a) Logarithm of the velocity, $\ln V$, and of the state, $\ln \Theta$. (b) Friction coefficient against non-dimensional time T. Result is shown for the 90% level and the 1 MPa/hr rate.

velocity becomes large and, thus, this term is not essential for failure. Including the Linker and Dieterich (1992) term decreases the magnitude of the jumps in velocity due to pore pressure jumps and delays the rapid increase in slip velocity. The onset of rapid slip is, however, more abrupt than for $\alpha = 0$. The delay is larger and the increase of velocity is more abrupt for the larger value of α. This very rapid increase in velocity is apparently the reason that the calculation does not converge for $\alpha = 0.4$ in (b) and (d). The more rapid increase of velocity with increasing α occurs because the Linker - Dieterich term effectively reduces the friction coefficient (Perfettini et al., 2001; Rice et al., 2001). Although the effect of this term on the critical stiffness (Segall & Rice, 1995) is small, it is significant here because of creep conditions: changes in effective normal stress caused by pore pressure changes occur at constant shear stress.

4. Other Pore Pressure Injection Programs

The calculations can be used to predict the results for programs of pore pressure increase other than that in the experiment. Here I briefly consider three: (a) linear increase; (b) ramp increase; and (c) periodic variation.

4.1. Linear Increase

The two stepwise pressure increases used by Scuderi et al. (2017) have the same average rate. Figure 9 compares the results of the stepped increases with those of a constant rate of the same magnitude. The result for the smaller steps, 0.2 MPa/12 min, is close to the constant rate. Calculations for progressively smaller steps would converge to the constant rate.

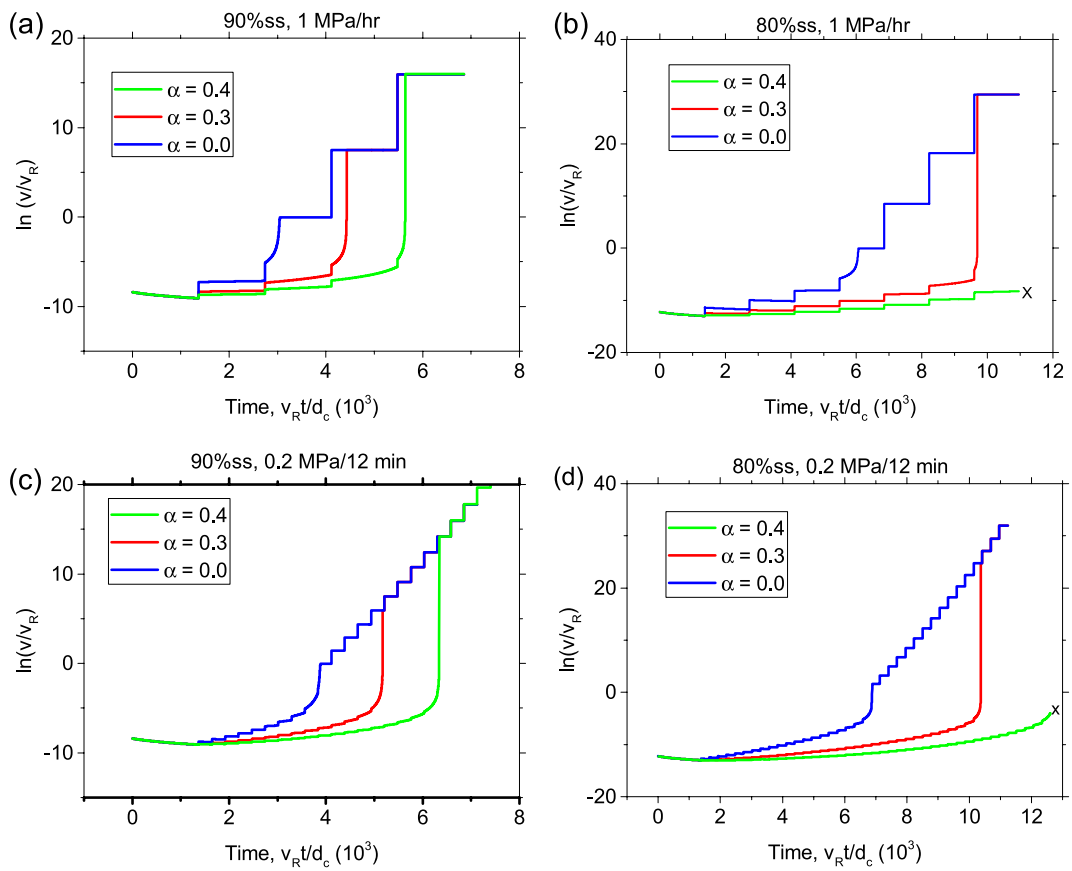

Figure 8. Dependence on the Linker and Dieterich (1992) term. Results are shown for $\alpha = 0.0$, 0.3, and 0.4.

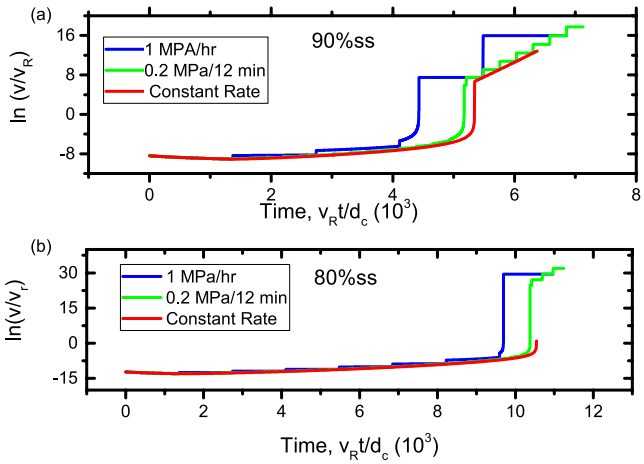

Figure 9. Comparison of a constant rate of pore pressure increase equal to the average of the two stepped increases, 1 MPa/hr and 0.2 MPa/12 min. Results for the 90% (a) and 80% (b) of steady state the stress level.

Figure 10 shows the effects of different constant rates for both the 90% and 80% of steady state stress levels. As expected, rapid slip occurs earlier for the higher rates. In addition, the approach to rapid slip occurs more gradually for the 80% of steady state level.

4.2. Ramp Increase

The inset of Figure 11 shows a ramp increase of pore pressure with a final (non-dimensional) value P_{final} and (non-dimensional) ramp time T_{ramp}. Results are shown for the 90% level. Figure 11a plots ln (v/v_R) versus T for $P_{\text{final}} = 0.05$, corresponding to 1 MPa and four ramp times 4, 6, 7.5, and 12 min (91.4, 137.1, 171.3, 274.1). As the ramp time gets larger, the rapid increase occurs later and less abruptly. For a ramp time of 12 min, the velocity stays well below v_R and for 7.5 min, it just reaches v_R. For a ramp time corresponding to 6 min the velocity increases to about 20 times v_R and for 4 min $10^7 v_R$. Figure 11b plots the response for a ramp time corresponding to 12 min and final pore pressures corresponding to 1, 1.5 and 2 MPa. Results are shown for the 90% level. For the 80% level and the same values for T_{ramp} and P_{final}, v stays orders of magnitude below v_R. The results indicate the strong dependence of both the pressure rate and pressure magnitude in causing rapid slip.

4.3. Periodic Pressure

A periodic variation of the pore pressure is given by $\Delta p(t) = \text{amp}\sin(2\pi t/t_p)$ where amp is the amplitude and t_p is the period. The non-dimensional form is $P(T) = A\sin(2\pi T/T_P)$ where $A = \text{amp}/\bar{\sigma}_0$ is the non-dimensional amplitude and $T_p = v_R t_p/d_c$ is the non-dimensional period.

Figures 12 and 13 show examples of the effects of pore pressure oscillation during creep conditions. Figure 12 shows results for a shear stress 90% of steady state and Figure 13 for 80%. Both figures show results for periods of 200 (a, b) and 100 (c, d); that is, 100 and 200 times the time scale of rate and state effects, d_c/v_R. Figure 12 shows results for two values of the pore pressure amplitude, 0.1 (a, c) and 0.15 (b, d); Figure 13 shows results for pore pressure amplitudes of 0.15 and 0.20. The black, dashed line and right axis show the pore pressure oscillation with amplitude normalized to 1. In all cases, ln(V) is periodic and the peaks slightly trail the peaks in pore pressure. For the smaller pore pressure amplitude in each figure, the peak velocity is less than the reference value; for the larger amplitude, the peak exceeds the reference velocity. The peaks in velocity are larger for the shorter period. Results for shorter periods are similar although the velocity variation is not always strictly periodic. Larger amplitudes show sharper peaks of velocity, but the calculations do not converge for amplitudes modestly larger than those shown. Because $P = p/\bar{\sigma}_0$, $P = 1$ corresponds to hydraulic fracture: the pore pressure equals the total normal stress. But, as noted, convergence issues arise well before this.

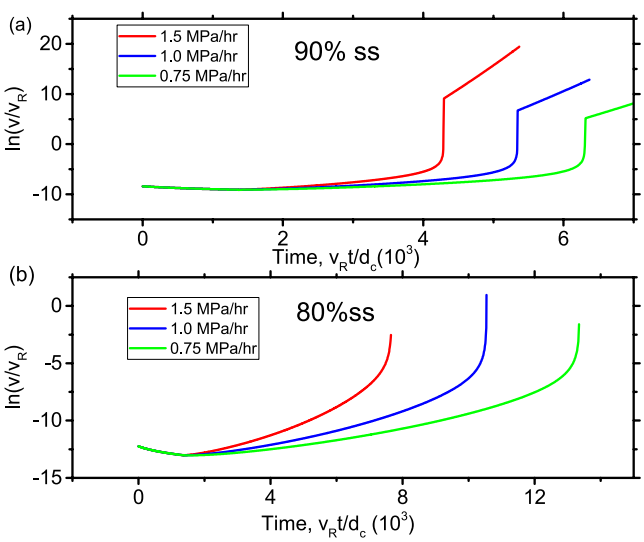

Figure 10. Ln (Velocity) versus Time for 90% level (a) and 80% level (b) for three pressure rates: 1.5 MPa/hr, 1.0 MPa/hr, and 0.75 MPa/hr.

5. Shale

Scuderi and Collettini (2018) have applied the same loading protocol for experiments on gouge formed from Rochester shale. The shale has a much lower nominal friction coefficient, is much more strongly velocity strengthening and has a much lower permeability.

5.1. Parameters

The parameters can be taken from Scuderi and Collettini (2018). As in Scuderi et al. (2017) the creep experiments were conducted at an initial effective normal stress of $\bar{\sigma}_0 = 20$ MPa and because they initially advance

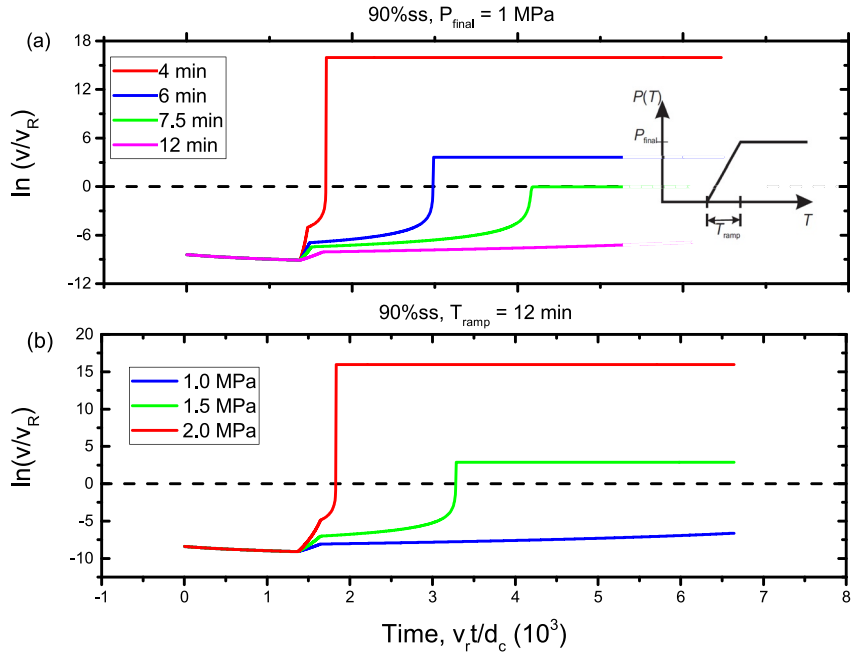

Figure 11. Ln (Velocity) versus Time for ramp increase of pore pressure (inset). (a) Results for a final pore pressure of 1 MPa for ramp times of 4, 6, 7.5 and 12 min (91.4, 137.1, 171.3, 274.1). (b) Results for a ramp time of 12 min and final pore pressures of 1, 1.5 and 2 MPa.

the ram at 10 μm/s, I again take this as the value of the reference velocity v_R. The steady state friction coefficient is $\mu_0 = 0.28$. For fluid injection at 1 MPa/hr, they observed a pore fluid equilibration time of 28–33 min. When Scuderi and Collettini (2018) convert these times to values of permeability (their Equation 8), they agree well with the permeability value measured in a separate test at $\bar{\sigma} = 20$ MPa, 9.76×10^{-20} m^2 (compared with $\sim 10^{-17}$ m^2 for the carbonate). This suggests using a equilibration time of 30 min, but I (see Figure 14) find that a value of about 10 min agrees better with the observations. Consequently, I use $c^* = 1/10$ min. I take $\beta = 1.0845 \times 10^{-6}$ m^2/N, the value given by Scuderi and Collettini (2018) as the compressibility of the gouge layer, assumed to be in the range of plastic to medium clay. Values of the frictional parameters a, b, and d_c were determined from velocity stepping tests in the range of velocities from 1 to 300 μm/s at effective normal stresses of 10, 16 and 20 MPa. Values vary with both the effective normal stress and the velocity (Scuderi & Collettini, 2018, Table 1). I take the values for $\bar{\sigma} = 20$ MPa and the velocity range 3–10 μm/s: $a = 0.0029$, $b = -0.0028$, and $d_c = 3.77$ μm. (I also tried values in the velocity range 10–30 μm/s: $a = 0.0039$, $b = -0.0044$, and $d_c = 16.74$ μm. Numerical results were slightly different but qualitatively similar.) Because the value of α must be less than the friction coefficient, I take $\alpha = 0.2$. I use the vertical machine stiffness, 386.12 kN/mm, and the area to calculate K. Because of the smaller value of d_c, $K = 0.024$. To extract the values of a, b, and d_c from the experimental measurements Scuderi and Collettini (2018) determined a stiffness for each experiment, which they give as in the range 0.005–0.008 μm^{-1}. When these are converted to units of kN/mm by multiplying by $\bar{\sigma} = 20$ MPa and the area (5.54 cm by 5.55 cm) the range is 307–492, which includes the value of the vertical machine stiffness. I take $\varepsilon = 1.7 \times 10^{-3}$, the value inferred by Segall and Rice (1995) from the data of Marone et al. (1990) on quartz gouge. The value for shale is likely different but there seems to be no guidance about what might be appropriate. The parameters are summarized in Table S2 (Supporting Information S1).

5.2. Results

Figure 14a shows the non-dimensional pore pressure in the reservoir, which increases at a rate of 1 MPa/hr (blue), and on the slip surface (red) as a function of non-dimensional time. Because the permeability is low the response is not fully drained and the increase of pore pressure on the slip surface lags that in the reservoir. More specifically, it approaches the pore pressure according to a diffusive curve. The graph shows that the pore pressure on the slip surface is nearly equal to that in the reservoir about half-way through the interval of constant pore pressure.

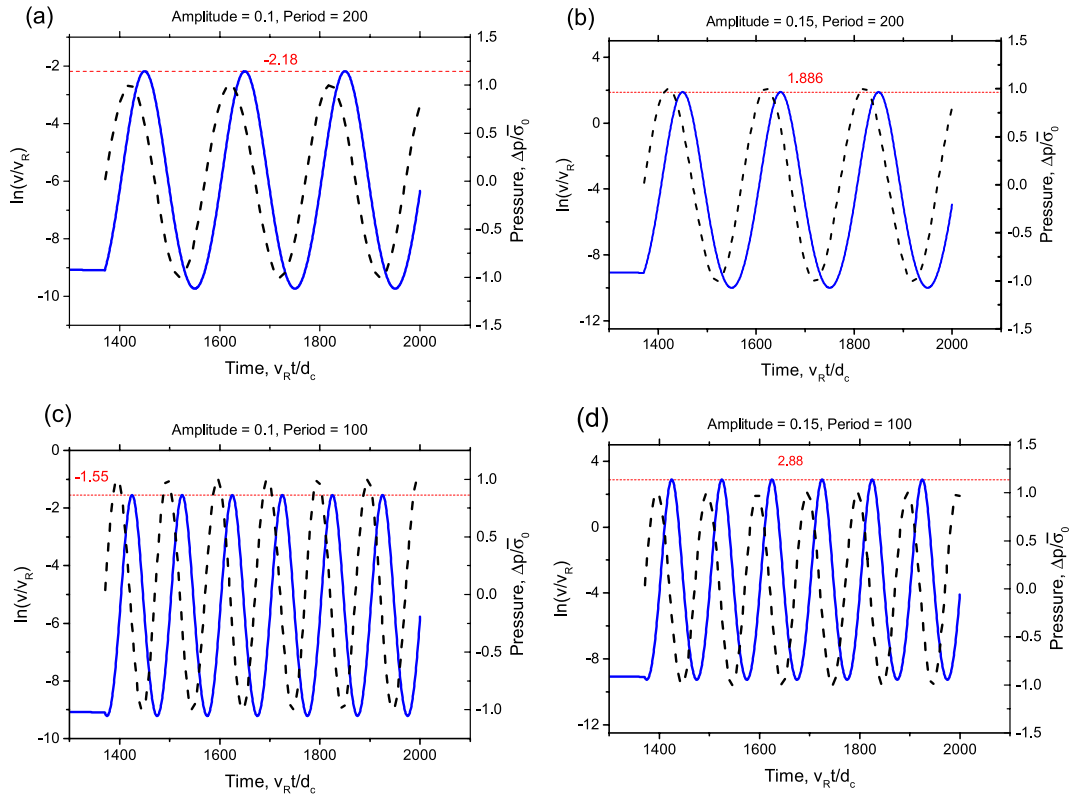

Figure 12. Each panel shows the logarithm of the non-dimensional velocity (in blue) and the pore pressure (in black, dashed and right axis, with magnitude normalized to 1), versus non-dimensional time. Results are for a stress level 90% of steady state. First column, (a) and (c), is for a pore pressure magnitude of 0.1 for periods of 200 (a) and 100 (c). Second column, (b) and (d), shows the results for a pore pressure magnitude of 0.15 and the same two periods of pore pressure variation. The horizontal red line marks the maximum of ln (V).

This agrees with the observed behavior (Scuderi & Collettini, 2018, Figure 10). As mentioned earlier in Subsection 5.1, the calculations use a diffusion time three times shorter (10 min rather than 30 min). With this value, halfway between the first and second jumps, the pore pressure on the slip surface is 95% of the reservoir pressure. If the larger value is used the time for equilibration is longer than the interval. For injection at 0.2 MPa per 12 min (Figure 14b), pore pressure equilibration occurs much closer to the end of the interval for constant reservoir pore pressure and the overall increase of pore pressure on the slip surface is roughly linear.

Figure 15 shows the calculated (red) and observed (blue) velocity on a log scale versus time for the four cases of stress equal to 80% or 90% of the steady state and for injection at 1 MPa/hr and 0.2 MPa/12 min. The calculated curves begin in the zero load point segment. Scuderi and Collettini (2018) do not show this segment. The origin is at the onset of the creep segment as in Figures 6 and 7 of Scuderi and Collettini (2018). Fluid injection begins at 60 min.

The spike in the graph of v for the pressure rate 1 MPa/hour is due to the jump in stress at constant state described by Equation 13. The large magnitude of the jump is the result of the very low friction coefficient. The stress $\tau = 4.56$ MPa at the end of the zero load point segment and for $a = 0.0029$ and $\mu_0 = 0.28$, the ratio of the velocity after the jump to that before is 3,671. For comparison, if $\mu_0 = 0.5$ with all other parameters the same, the stress at the end of the zero load point segment is 8.96 MPa and the ratio of the velocity after to that before is 1.86. Scuderi and Collettini (2018) only show results from the beginning of the creep segment so it is not possible to tell whether a similar feature occurred in the experiment. The spike is so short in duration it conceivably could be missed in the experiment although this seems unlikely for such a dramatic feature. In any case, because the specimen creeps at constant stress for an hour before injection begins, the jump appears to have little effect on the ensuing response.

The second column of Figures 15b and 15d shows results for the velocity versus time at the 80% of steady state stress level. Because the stress decreases from the end of the zero load point segment and is a smaller percentage of the steady state level, there is no spike in the velocity at the beginning of creep segment for the calculated

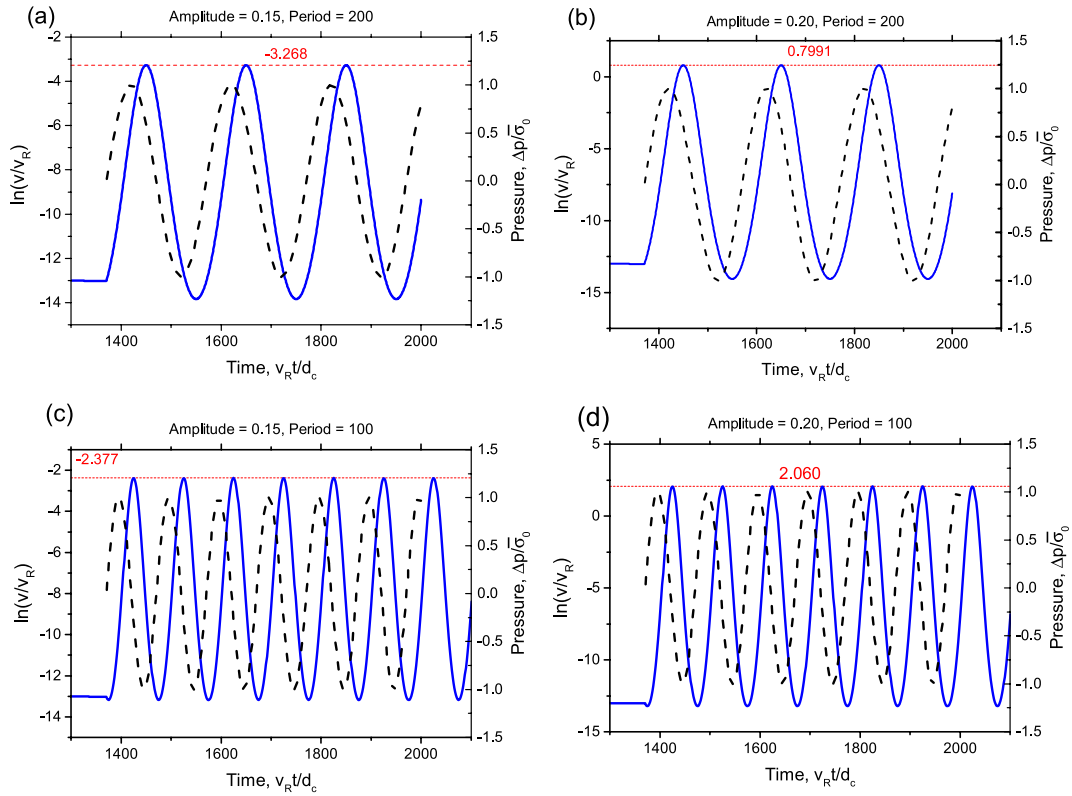

Figure 13. Each panel shows the logarithm of the non-dimensional velocity (in blue) and the pore pressure (in black, dashed and right axis, with magnitude normalized to 1) versus non-dimensional time. Results are for a 80% reduction in stress. First column, (a) and (c), is for a pore pressure magnitude of 0.15 for periods of 200 (a) and 100 (c). Second column, (b) and (d), shows the results for a pore pressure magnitude of 0.2 and the same two periods of pore pressure variation. The horizontal red line marks the maximum of ln (V).

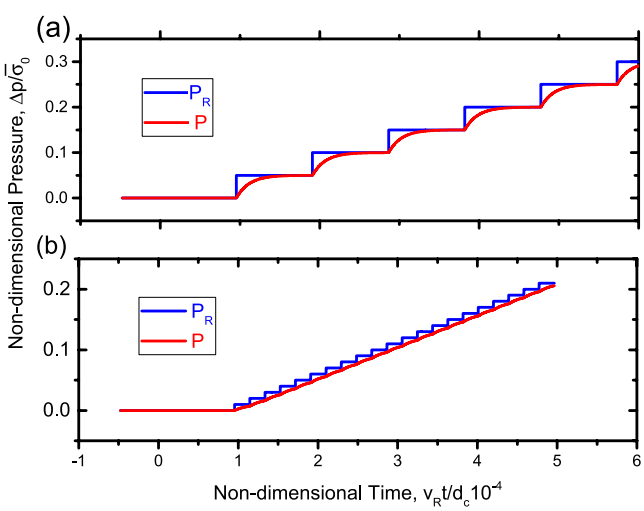

Figure 14. The (non-dimensional) pore pressure increase in the reservoir (blue) and on the slip surface (red) as a function of (non-dimensional) time for $c^* = 1/10$ min. Pore pressure increases at (a) 1 MPa/hr and (b) 0.2 MPa/12 min.

results. On the contrary, there is a small decrease in velocity at the beginning of the pore pressure increase before the rapid increase.

For the 90% stress level, as expected, the observed curves of the velocity and displacement for 1 MPa/hour injection rate occur earlier than for the 0.2 MPa/12 min rate. Surprisingly, for the 80% the dependence is reversed (Figures 6 and 7 of Scuderi and Collettini (2018)).

The first row of Figure 15 shows the results for the pore pressure increase at 0.2 MPa/12 min and both levels of stress. For the 90% stress level the velocity jumps are small but discernible on the observed curve. The velocity increases rapidly at 240 min (This would be at the fifteenth jump in reservoir pore pressure.) up to 0.2 mm/s. For the 80% level, the observed curve seems to have little correlation with the pore pressure increases. There is a slight increase at the beginning of injection (60 min), a decrease until 130 min, a roughly linear increase until 250 min. Finally, there is a slight increase until a rapid increase around 300 min to a velocity of 0.18 mm/s at 311 min. The calculated curves increase linearly from the onset of injection and do not show a rapid upturn. Nevertheless the calculated velocity at the 90% level (0.06 mm/s) is not significantly less than the final observed value. For the 80% stress level, the calculated and observed velocities intersect at 308 min (2.9 μm/s), but the calculated value (3.7 μm) at the time of the final observed value is a factor of 50 smaller. In both cases the final observed velocities are small.

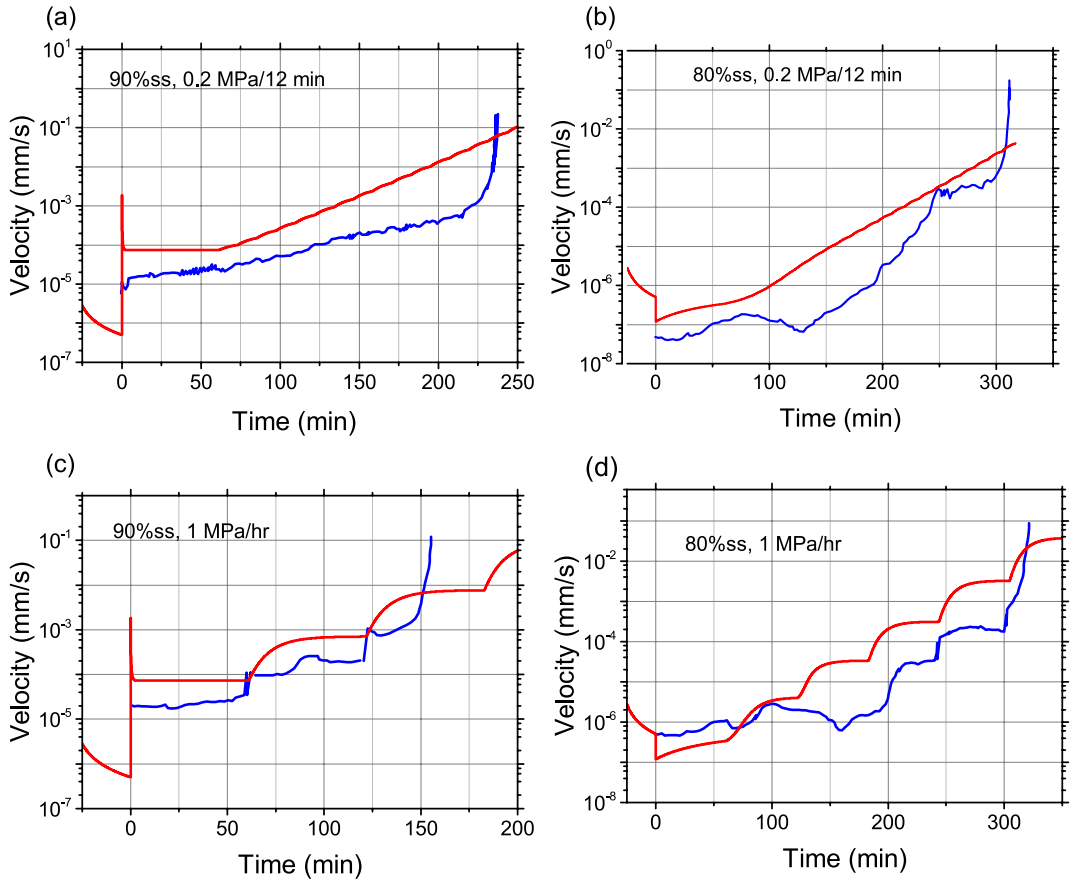

Figure 15. The figure shows the observed velocity versus time for the calculations (red) and for the observations (blue). The curves for the observations were digitized from Figures 6 and 7 of Scuderi and Collettini (2018). The first column, (a) and (c), shows results for the shear stress at 90% of the steady state value and the second column for 80% of steady state. The first row, (a) and (b), shows results for the 0.2 MPa/min injection rate and the second, (c) and (d), for the 1 MPa/hr rate.

The second row (Figures 15a and 15b) shows the results for pore pressure increase of 1 MPa/hr and both stress levels. For the 90% level, the calculations show a rapid increase in the velocity just after a jump in reservoir pressure followed by a slowly increasing segment. This pattern repeats itself. For the 90% level the experimental results show a rapid increase of the velocity after injection starts and a leveling off but then a more gradual rise and another plateau until the second jump in reservoir pressure at 120 min. The observed velocity after the second pore pressure increase also shows a sudden increase and a plateau but then a continuous rapid increase before the time of the third jump of reservoir pressure (180 min). In contrast the calculation is leveling off at this time. Nevertheless, velocities are similar for the experiment and calculation at the same time. After the initial injection at 60 min, the calculated velocity levels off at 0.703 μm/s just before the second increase in reservoir pressure at 120 min. The observed value just before the second increase is about 0.2 μm/s. After the second increase, the calculated velocity levels off at 7.62 μm/s just before the third increase at 180 min. In the experiment, the velocity after the second jump does not plateau but dips slightly and then increases rapidly to about 100 μm/s when the graph ends at about 155 min. This is only 10 times the reference velocity. At this time in the calculation, the velocity is 6.99 μm/s and a velocity of 100 μm/s is not reached until 244 min.

Figure 16 shows the measured and calculated displacements for the four cases. For pore pressure increase of 1 MPa/hr and the 90% stress level, Figure 16c, both the calculated and measured curves are roughly linear, though slightly offset, until the observed displacement increase becomes nearly vertical on the scale of the graph at about 150 min. This rapid increase is consistent with the rapid increase in slip velocity at about the same time. At 120 min, the calculated displacement is 2.13 mm compared with 1 mm in the experiment. The observed displacement then rises quickly and is 10 mm when the graph ends at 155 min. At this time, the calculated displacement is 11 mm.

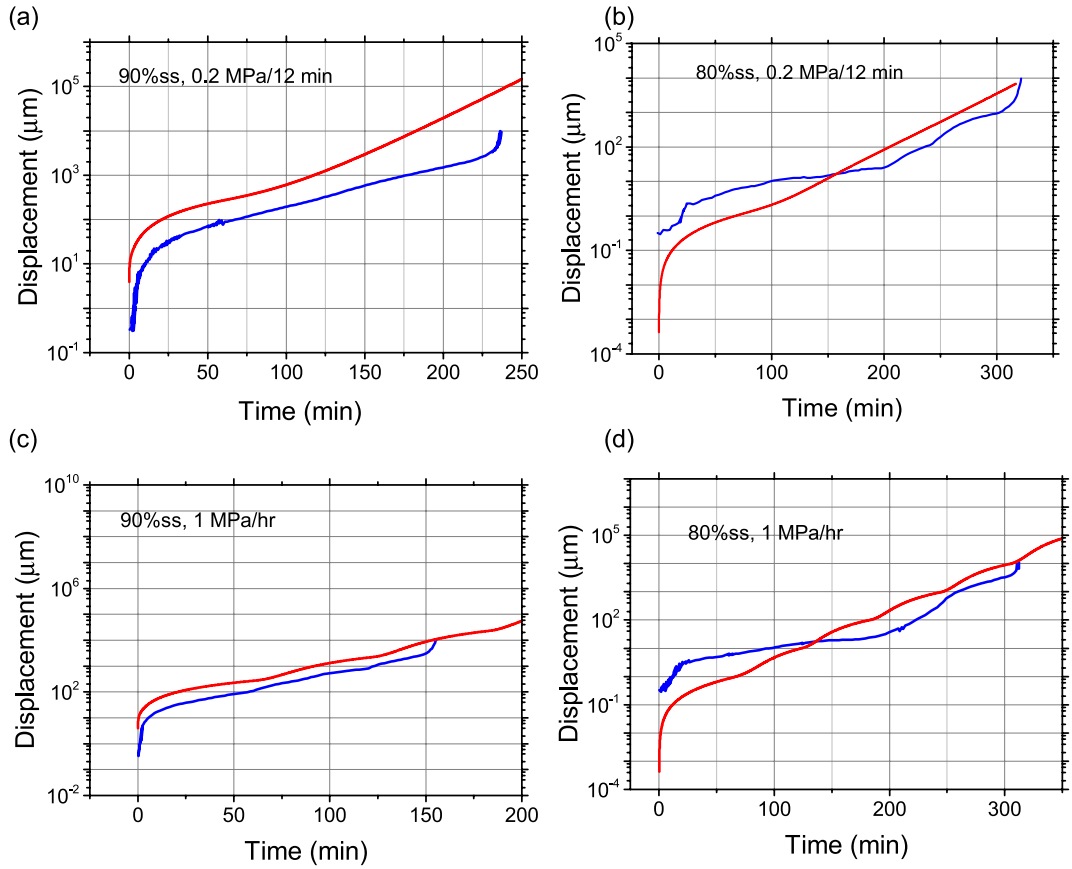

Figure 16. The figure shows the observed displacement versus time for the calculations (red) and for the observations (blue). The curves for the observations were digitized from Figures 6 and 7 of Scuderi and Collettini (2018). The first column, (a) and (c), shows results for the shear stress at 90% of the steady state value and the second column for the 80% of steady state. The first row, (a) and (b), shows results for the 0.2 MPa/min injection rate and the second, (c) and (d), for the 1 MPa/hr rate.

For the 90% stress level and lower pressure rate (Figure 16a) both the calculated and measured displacements are linear after injection, but the calculated curve is offset and has a slightly large slope. The observed displacement has a rapid increase to a displacement of about 10 mm at 236 min. The calculated displacement is substantially larger, about 83 mm, and is increasing at a much lower rate. For the 80% stress level the measured displacement for both pressure rates increases slowly until 180 min, then more rapidly, and, finally, nearly vertical on the plot at a little more than 300 min. The largest slip values plotted are close to 5 mm. The simulation values are about the same at this time, although the measured curves are increasing much more rapidly than the calculated ones.

6. Discussion

This study has used a spring block model with rate and state friction to simulate experiments on carbonate gouge (Scuderi et al., 2017) and on shale-containing gouge (Scuderi & Collettini, 2018). Both experiments are conducted with the same loading protocol: stepwise increase of pore fluid pressure under creep conditions (constant shear stress). Both the carbonate gouge and the shale are velocity strengthening, the shale strongly so. For the carbonate gouge, the calculated curves have the general shape of a creep curve, as observed. Furthermore, the calculated onset of rapid velocity and slip agrees well with the identification of tertiary creep in the experiment.

The material characteristics of the shale are significantly different from those of the carbonate. The shale has a very low nominal coefficient of friction ($\mu_0 = 0.28$) and the rate and state parameter b is less than zero. The latter changes the sign of the Linker and Dieterich (1992) term in Equation 7. The low friction coefficient leads to some unusual responses in the simulation, namely, the spike following the zero load point segment when the shear stress is increased to 90% of the steady state level and the slight decrease in the slip velocity immediately

following the beginning of fluid pressure increase in the tests at 80% of the steady state level. For the 80% of steady state stress level, values of the velocity and displacement occur earlier for the 0.2 MPa/12 min rate than equal values for the 1 MPa/hr rate. The observed curves also have some inconsistencies with the pattern of rising pore pressure (except for the lower pressure rate and the 90% of steady state stress level). These are decreasing portions and rapidly rising portions that do not correlate with rapid rises in pore pressure.

The shale is strongly velocity strengthening. Although the observed velocity is rising rapidly at the end of the experiment, the velocities remain small, at most about 10 times the reference velocity. The calculated velocities are also still rising at the time the experiment ends, but at a much smaller rate and the velocities are smaller than those observed. That both the calculated and observed velocities are still rising at the end of experiment begs the question of whether they would become significantly larger if the experiment went longer. Although there are numerous other factors that can play a role in field applications, the possibility of continued increase of slip velocity suggests that long-time pore fluid increase could trigger rapid slip even when the behavior is strongly velocity strengthening. The calculated displacements at the end of the experiment agree well with the observed displacements (except for the lower injection rate for the 90% of steady state stress level) although the observed displacements are increasing much more rapidly than the calculated.

The relatively good agreement of the calculations with some features of the observations indicates that rate and state friction does account for aspects of the response, particularly failure. Overall, however, there are significant differences between the observed and calculated curves for both the carbonate and the shale. This is not surprising. It would be unrealistic to expect that all aspects of the deformation are accounted for by rate and state friction. There are likely other mechanisms involved. For the carbonate there is bulk creep. A possible factor for both materials is direct dependence on the slip itself in addition to dependence on velocity and state. Also, the measured rate and state parameters varied with velocity and normal stress and, in some cases, required two state variables for an adequate description. A few simulations for different values of the rate and parameters did not indicate significant differences but a dependence on velocity would change the shapes of the velocity and displacement curves. Perhaps more importantly, for both the carbonate and shale, the evolving structure of the gouge is likely to play a role.

Both Scuderi et al. (2017) and Scuderi and Collettini (2018) discuss microstructural observations that indicate evolution of the gouge structure. For the carbonate, microstructural observations indicate grain size reduction and cataclasis with shear, localization on planar surfaces, and evidence of pressure solution and dissolution. For the shale, Scuderi and Collettini (2018) note that small variations in starting porosity strongly influence frictional and hydraulic properties and slip. As for the carbonate, shearing is accompanied by cataclasis and grain size reduction and the development of localized shear planes. Localized shearing of illite layers is likely the cause of the very low frictional strength. Moreover, narrow bands of illite can locally create strong permeability barriers and lead to overpressures. These microstructural features are absent from the spring block simulation. The pore fluid pressure is uniform in the narrow gouge zone and the exchange of fluid with the reservoir is simply proportional to the pressure difference. An improved model, though one that still is not a good characterization of the microscale, would include a finite thickness gouge layer in which fluid diffusion occurs and which exchanges fluid with the surrounding material. Heimisson et al. (2021, 2022) have formulated and numerically evaluated a plane strain model of this type.

Ruina (1983) has analyzed the stability of slip for drained conditions (constant pore pressure) at constant shear stress. He shows that for velocity strengthening the slip velocity quickly becomes unbounded for velocity weakening friction $b > a$ and rapidly decays for velocity strengthening. His analysis used the slip law for evolution of the state variable but a linearized perturbation analysis about steady state sliding for the aging law arrives at the same conclusion. Perturbations grow exponentially for velocity weakening and decay for velocity strengthening.

The simulations for the carbonate gouge reinforce the experimental observation that the analysis of Ruina (1983) does not apply when the pore pressure is increasing: increase of pore fluid pressure can cause rapid slip under creep conditions even in a velocity strengthening material. The calculations for carbonate agree well with the time and displacement at the onset of tertiary creep identified in the experiment. For the carbonate gouge, the permeability is large enough that the changes of pore pressure on the slip surface are essentially the same as the imposed step wise pore pressure increase. In this case, the effect of the pore pressure increase in increasing the slip velocity is seen from Equation 15. If the equation is specialized to a series of steps in pore pressure, the velocity after the kth jump is given by

$$V_{k+1} = V_k \left(\frac{1 - P_{k+1}}{1 - P_k} \right)^{\alpha/a} \exp\left\{ \frac{P_{k+1} - P_k}{a(1 - P_{k+1})} \mu(V_k, \Theta_k) \right\} \quad (16)$$

Although the first term (…) decreases with an increase in pressure, it is outweighed by the increase in the argument of the exponential. Thus, the decrease in effective compressive stress due to pore pressure increase does play a role in increasing the slip velocity under creep conditions. Equation 16 applies for drained conditions and step wise increases of pore pressure. For lower permeability, pore pressure changes on the slip surface are modulated by diffusion which delays the increase in slip and velocity. Nevertheless, the basic mechanism is expected to be the same.

Scuderi et al. (2017) argue that for pore pressure increase there is a competition between stabilizing effects of rate and state friction, because of velocity strengthening, and a reduction in the effective normal stress. They suggest that the rapid slip occurs because the increase in pore pressure overcomes the second order effects of rate and state friction. In essence this is described by Equation 16. But the calculations indicate that failure corresponding to rapid slip arises purely from the rate and state framework without the need to impose a separate Mohr-Coulomb condition. Nevertheless, for the carbonate gouge, the agreement between calculations and observations suggests that the onset of rapid slip in the rate and state simulation is consistent with the prediction of failure when the effective compressive stress reaches a Mohr-Coulomb failure line. Observations for the shale do not agree with failure according to the Mohr-Coulomb condition (Scuderi & Collettini, 2018).

At least for creep conditions, the calculations here resolve an apparent discrepancy between the effect of pore pressure increase on the Mohr-Coulomb condition and on rate and state friction (as pointed out by Scuderi et al., 2017 and others). An increase in pore pressure reduces the effective normal stress and, consequently, the frictional resistance. This promotes slip. However, within the rate and state formulation, an increase in pore pressure reduces the critical stiffness (Equation 6). This lowers k_{crit} which is a stabilizing effect. But the spring constant plays no role for creep loading. It appears in the formulation here only in the calculation for the zero load point segment. Consequently, the reduction of the critical spring stiffness due to an increase in pore pressure is not a factor.

An added value of the simulations is that they can be used to examine pore pressure increases that differ from those used in the experiment. The calculation shown in Figure 9 for a linear increase confirms the intuitive expectation that the step wise loading used in the experiment approaches the linear increase for decreasing magnitude and shorter duration of steps. Figure 11 for the ramp loading shows that whether pore pressure increase induces rapid slip under creep conditions depends on the magnitude, rate, and duration of loading. This is a result that is relevant to controlling fluid injection parameters to avoid inducing seismicity. Almakari et al. (2019) have used a continuum model to calculate seismicity resulting from injection of fluid described by a ramp increase of pore pressure. The frictional behavior on the fault is described by a distribution of both velocity weakening and velocity strengthening patches. They find that increasing the maximum pore pressure increases the magnitude and duration of the seismicity rate but decreases the frequency of large magnitude events. Increase of the pore pressure rate also increases the seismicity rate up to a critical pressure rate. For larger rates, large magnitude events are more frequent.

A few examples of periodic loading were presented in Figures 12 and 13. For the two amplitudes and periods considered, the slip velocity is periodic and the peaks slightly follow the peaks in pore pressure. Periodic variations of pore pressure can be due to a variety of mechanisms including tidal loading and seasonal variations in water storage, or reservoir filling. There have been several experimental studies of periodic pore pressure variations on intact samples (Chanard et al., 2019; Farquharson et al., 2016; Noël, Pimienta, & Violay, 2019; Zhuang et al., 2016). Noël, Passelégue, et al. (2019) conducted axisymmetric compression tests on a saw cut sample of Fountainebleau sandstone subjected to periodic pressure changes. They found that acoustic emission and stick slip events clustered around peaks in pore pressure. Rudnicki and Yu (2021) made simulations using a spring block model with periodic pore pressure (assuming constant total normal stress which is not the case for axisymmetric loading). For constant values of the rate and state parameters a, b, and d_c, they found a more varied behavior (albeit with an arbitrarily chosen value for the ratio of the spring stiffness to the critical value given by Equation 6). For some cases slip velocity peaks occurred near pore pressure peaks, but not at every pore pressure peak and in other cases the peaks occurred closer to the troughs. The observations of Noël, Passelégue, et al. (2019) showed that the rate and state parameters varied with increases in slip velocity in a manner that was

destabilizing because it increased the critical value of the spring constant. When this variation was included in the simulation, slip oscillation caused the critical value to vary about the spring stiffness and stability depended on the length of time that k stayed below the critical value. In addition, the results were strongly dependent on the amplitude of the periodic variation.

Figure 8 examined the effect of the Linker and Dieterich (1992) term Equation 7. Segall and Rice (1995) derived an expression for the change in the critical value of the spring constant due to including α for undrained conditions. Their derivation indicated that the effect is small. However, Figure 8 shows that the effect is important for changes of effective stress due to the pore pressure injection under creep conditions. More specifically, Figure 8 shows that increasing values of α lead to a later, but more abrupt, occurrence of rapid slip. But even when $\alpha = 0$ the slip velocity grows, a result that is consistent with Equation 16. Because changes of pore pressure in the slipping region for the carbonate simulations are the same as in the reservoir, the Linker and Dieterich (1992) effect is entirely due to the alteration in state caused by a jump in effective compressive stress, Equation 14. Andrés et al. (2019) have also emphasized the importance of this effect in initiating slip on dormant faults.

The formulation here uses that of Linker and Dieterich (1992), expressed by the term in Equation 7. However, a more recent study of normal stress effects (Kilgore et al., 2017) indicates that the Linker and Dieterich (1992) study is in need of revision. Among the results of Kilgore et al. (2017) is that a sudden change in normal stress does not cause a sudden change in slip rate as in the Linker and Dieterich (1992) formulation. Instead the change in slip rate evolves to a new value along an exponential curve with a characteristic slip distance that is significantly smaller than d_c. The much smaller characteristic slip distance suggests that a step jump might be a good approximation. However, Ranjith and Rice (1999) and Rice et al. (2001) found that formulations with any constitutive equation that allows a sudden change in shear resistance accompanying a normal stress change are unstable and have no solution. That is not the case here. The calculations (Figure 5) show that jumps in normal stress due to pore pressure increase are accompanied by jumps in velocity, at least when α is not too big. The failure of the calculation to converge for $\alpha = 0.4$ (Figures 8b and 8d) may be an indication of the instability identified by Ranjith and Rice (1999) and Rice et al. (2001). The difference between their results and those here may be due to the different loading conditions. The analyses of Ranjith and Rice (1999) and Rice et al. (2001) were for perturbations from steady state; those here are for creep at constant shear stress.

Calculations using the exponential approach to a new velocity level following a sudden change in normal stress would undoubtedly have some differences from those here. But the differences probably would not alter the overall behavior of the response. In view of the lack of detailed agreement of the calculated curves with the experimental ones, the differences would not seem to be significant.

Although changes in porosity are not shown, the evolution in the calculations varies as $\ln(V)$, as expressed by Equation 8. In both the experiments and the calculations for the carbonate gouge, there is slow, slight compaction prior to tertiary creep. Creep rates in this period are greater for the 90% level of steady state stress by roughly a factor of two, consistent with the experiment. The compaction is followed by a sharp increase in dilation accompanying the rapid increase in slip velocity corresponding with tertiary creep. In the calculations, the rapid dilation is not, however, succeeded by rapid compaction as seen in the experiment. The porosity change never gets large, at most a few times 10^{-3}. Scuderi et al. (2017) report values of the change in layer thickness which is a proxy for the change in porosity. The magnitude of the calculated change in porosity is similar to the percentage change in layer thickness, a few tenths of a percent at the onset of tertiary creep.

For the shale, the observations show compaction in the creep state prior to the beginning of injection. Injection causes dilation in both the experiment and the observations. Dilation continues in the calculation but the experiments show a change from dilation to compaction. Although the detailed variation of the volume changes is different for the experiments and calculations, the magnitude of the porosity changes are similar. Scuderi and Collettini (2018) report a dilation of the layer of 0.17%–0.3% of the initial layer thickness. Also, for the shale, Scuderi and Collettini (2018) document a dependence of the volume changes on the initial density. The calculations do not, however, depend on the initial porosity.

The spring stiffness k does not enter for the creep calculations. It enters only in the zero load point segment. Most experiments are done with constant load point velocity instead of constant shear stress. Simulations of such experiments do involve the spring stiffness. Rudnicki and Zhan (2020) have used a spring block model to examine the effect of pressure rate on rate and state frictional slip. They primarily use parameters from French

et al. (2016) although French et al. (2016) did not provide a value for the stiffness. Also, the calculations assumed constant total normal stress which is not the case in axisymmetric compression experiments. The pressure rate was assumed to be constant. Rudnicki and Zhan (2020) found that the frequency of rapid slip events increases with the ratio of the time scale of frictional sliding to that for pressure increase. As the pressure rate increases, the increase of k_{crit}, Equation 6, because of the rapid increase of pore pressure on the slip surface quickly stabilizes slip due to rate and state friction. For low diffusivities, dilatant hardening (Segall & Rice, 1995) limits rapid slip velocities. Rate and state effects interact in a limited range of pressure rate and diffusivity that includes those representative of recent experiments.

Alghannam and Juanes (2020) have also used a spring block model to examine the effects of injection rate a constant rate of pore pressure. They include a spring perpendicular to the slip plane that simulates poroelastic effects. They also emphasize the importance of the pore pressure rate. In particular, they found that the rate of increase of pore pressure is more important than the pore pressure itself for triggering earthquakes. These results are consistent with that of the continuum simulation by Almakari et al. (2019) mentioned earlier. The calculations are also consistent with the observations of Weingarten et al. (2015). They looked at about 20,000 wells associated with seismicity and found that among a various operational parameters the effect of injection rate had the best correlation with induced seismicity. In particular, they found that the number of events was correlated with the maximum rate than with the injected volume.

7. Conclusion

This study has used a simple spring block model with rate and state friction to simulate experiments on carbonate gouge and shale under constant shear stress (creep) conditions with pore fluid increases. Both materials are velocity strengthening, the shale strongly so. The onset of rapid slip in the calculations agrees well with the identification of tertiary creep for the carbonate gouge. This result reinforces the observation that increase in pore pressure can cause rapid slip events even for a velocity strengthening material. The development of rapid slip is an intrinsic result of rate and state friction and the imposition of a Mohr - Coulomb condition is unnecessary. For the shale, both the calculations and experiments show very small velocity increases by the end of the experiment although the calculated velocities and their rate of increase are significantly less than the observed. The calculated and observed displacements agree well at the end of the experiment although, again, the rate of increase for the calculated curves is much less than the observed.

Data Availability Statement

Annotated Mathcad (PTC,Inc) worksheets and all output files are available at https://doi.org/10.5281/zenodo.7793232.

Acknowledgments
I am grateful for financial support from the National Science Foundation Geophysics Program through award number EAR-2120374. This study was started while I was visting École Normal Supérieure in Paris and I am grateful for their hospitality and support. Thanks to Chris Marone for suggesting that I look at the Scuderi et al. (2017) study. Thanks to Marco Scuderi for providing some rate and state friction data and clarifying some aspects of the study. Also, thanks to Marco for bringing the shale paper to my attention and suggesting that I look at that data, as well. Finally, thanks to the AE, an anonymous reviewer and Eric Dunham. Their helpful comments and suggestions led to significant improvements of the paper.

References

Ake, J. K., O'Connell, D., & Block, L. (2005). Deep-injection and closely monitored induced seismicity at Paradox Valley, Colorado. *Nature Communications*, *95*(1), 3053–683. https://doi.org/10.1785/0120040072

Alghannam, M., & Juanes, R. (2020). Understanding rate effects in injection-induced earthquakes. *Nature Communications*, *11*(1), 3053. https://doi.org/10.1038/s41467-020-16860-y

Almakari, M., Dublanchet, P., Hervé, C., & Frédéric, P. (2019). Effect of the injection scenario on the rate and magnitude content of injection-induced seismicity: Case of a heterogeneous fault. *Journal of Geophysical Research*, *124*, 8426–8448. https://doi.org/10.1029/2019jb017898

Ampuero, J.-P., & Rubin, A. M. (2008). Earthquake nucleation on rate and state faults–aging and slip laws. *Journal of Geophysical Research*, *113*(B1). https://doi.org/10.1029/2007jb005082

Andrés, S., Santillán, D., Mosquera, J. C., & Cueto-Felgueroso, L. (2019). Delayed weakening and reactivation of rate-and-state faults driven by pressure changes due to fluid injection. *Journal of Geophysical Research: Solid Earth*, *124*(11), 11917–11937. https://doi.org/10.1029/2019JB018109

Barbour, A. J., Norbeck, J. H., & Rubinstein, J. L. (2017). The effects of varying injection rates in Osage county, Oklahoma, on the 2016 Mw 5.8 Pawnee earthquake. *Seismological Research Letters*, *88*, 1040–1053.

Bhattacharya, P., Rubin, A. M., Tullis, T. E., Beeler, N. M., & Okazaki, K. (2022). The evolution of rock friction is more sensitive to slip than elapsed time, even at near-zero slip rates. *Proceedings of the National Academy of Sciences*, *119*(30), e2119462119. https://doi.org/10.1073/pnas.2119462119

Bourouis, S., & Bernard, P. (2007). Evidence for coupled seismic and aseismic fault slip during water injection in the geothermal site of Soultz (France), and implications for seismogenic transients. *Geophysical Journal International*, *169*(2), 723–732. https://doi.org/10.1111/j.1365-246x.2006.03325.x

Brantut, N., Heap, M., Meredith, P., & Baud, P. (2013). Time-dependent cracking and brittle creep in crustal rocks: A review. *Journal of Structural Geology*, *52*, 17–43. https://doi.org/10.1016/j.jsg.2013.03.007

Byerlee, J. (1990). Friction, overpressure and fault normal compression. *Geophysical Research Letters*, *17*(12), 2109–2112. https://doi.org/10.1029/gl017i012p02109

Cappa, F., Scuderi, M. M., Collettini, C., Guglielmi, Y., & Avouac, J.-P. (2019). Stabilization of fault slip by fluid injection in the laboratory and in situ. *Science Advances*, *5*, eaau4065. https://doi.org/10.1126/sciadv.aau4065

Chambon, G., & Rudnicki, J. W. (2001). Effects of normal stress variations on frictional stability of a fluid-infiltrated fault. *Journal of Geophysical Research*, *106*(B6), 11353–11372. https://doi.org/10.1029/2001jb900002

Chanard, K., Nicolas, A., Hatano, T., Petrelis, F., Latour, S., Vinciguerra, S., & Schubnel, A. (2019). Sensitivity of acoustic emission triggering to small pore pressure cycling perturbations during brittle creep. *Geophysical Research Letters*, *46*(13), 7414–7423. https://doi.org/10.1029/2019gl082093

Charéty, J., Cuenot, N., Dorbath, L., Dorbath, C., Haessler, H., & Frogneux, M. (2007). Large earthquakes during hydraulic stimulations at the geothermal site of Soultz-sous-Forêts. *International Journal of Rock Mechanics and Mining Sciences*, *44*, 1091–1105.

Collettini, C., & Sibson, R. (2001). Normal faults, normal friction? *Geology*, *29*(10), 927–930. https://doi.org/10.1130/0091-7613(2001)029<0927:nfnf>2.0.co;2

Cueto-Felgueroso, L., Santillán, D., & Mosquera, J. C. (2017). Stick-slip dynamics of flow-induced seismicity on rate and state faults. *Geophysical Research Letters*, *44*(9), 4098–4106. https://doi.org/10.1002/2016GL072045

Cueto-Felgueroso, L., Vila, C., Santillán, D., & Mosquera, J. C. (2018). Numerical modeling of injection-induced earthquakes using laboratory-derived friction laws. *Water Resources Research*, *54*(12), 9833–9859. https://doi.org/10.1029/2017WR022363

Deichmann, N., & Giardini, D. (2009). Earthquakes induced by the stimulation of an enhanced geothermal system below basel (Switzerland). *Seismological Research Letters*, *80*(5), 784–798. https://doi.org/10.1785/gssrl.80.5.784

Dieterich, J. H. (1979). Modeling of rock friction: 1. Experimental results and constitutive equations. *Journal of Geophysical Research*, *84*(B5), 2161–2168. https://doi.org/10.1029/jb084ib05p02161

Dieterich, J. H. (1980). Experimental and model study of fault constitutive properties. *Solid Earth Geophysics and Geotechnology*, *42*, 21–29.

Dieterich, J. H. (1986). A model for the nucleation of earthquake slip. *Earthquake source mechanics*, *37*, 37–47.

Dieterich, J. H. (1992). Earthquake nucleation on faults with rate-and state-dependent strength. *Tectonophysics*, *211*(1–4), 115–134. https://doi.org/10.1016/0040-1951(92)90055-b

Dublanchet, P. (2019). Fluid driven shear cracks on a strengthening rate-and-state frictional fault. *Journal of the Mechanics and Physics of Solids*, *132*, 103672. https://doi.org/10.1016/j.jmps.2019.07.015

Ellsworth, W. L. (2013). Injection-induced earthquakes. *Science*, *341*. https://doi.org/10.1126/science.1225942

Evans, K. F., Zappone, A., Kraft, T., Deichmann, N., & Moia, F. (2012). A survey of the induced seismic responses to fluid injection in geothermal and CO_2 reservoirs in Europe. *Geothermics*, *41*, 30–54. https://doi.org/10.1016/j.geothermics.2011.08.002

Farquharson, J., Heap, M. J., Baud, P., Reuschlé, T., & Varley, N. R. (2016). Pore pressure embrittlement in a volcanic edifice. *Bulletin of Volcanology*, *78*, 1–19. https://doi.org/10.1007/s00445-015-0997-9

Faulkner, D. R., & Rutter, E. H. (2001). Can the maintenance of overpressured fluids in large strike-slip fault zones explain their apparent weakness? *Geology*, *29*(6), 503–506. https://doi.org/10.1130/0091-7613(2001)029<0503:ctmoof>2.0.co;2

French, M. E., Zhu, W., & Banker, J. (2016). Fault slip controlled by stress path and fluid pressurization rate. *Geophysical Research Letters*, *43*, 4330–4339. https://doi.org/10.1002/2016GL068893

Frohlich, C. (2012). Two-year survey comparing earthquake activity and injection-well locations in the Barnett Shale, Texas. *Proceedings of the National Academy of Sciences*, *109*(35), 13934–13938. https://doi.org/10.1073/pnas.1207728109

Frohlich, C., Ellsworth, W., Brown, W. A., Brunt, M., Luetgert, J., MacDonald, T., & Walter, S. (2014). The 17 May 2012 M4. 8 earthquake near Timpson, East Texas: An event possibly triggered by fluid injection. *Journal of Geophysical Research: Solid Earth*, *119*(1), 581–593. https://doi.org/10.1002/2013jb010755

Garagash, D. I. (2021). Fracture mechanics of rate-and-state faults and fluid injection induced slip. *Philosophical Transactions of the Royal Society A*, *379*, 20200129. https://doi.org/10.1098/rsta.2020.0129

Garagash, D. I., & Germanovich, L. N. (2012). Nucleation and arrest of dynamic slip on a pressurized fault. *Journal of Geophysical Research*, *117*(B10319). https://doi.org/10.1029/2012JB009209

Gori, M., Rubino, V., Rosakis, A. J., & Lapusta, N. (2021). Dynamic rupture initiation and propagation in a fluid-injection laboratory setup with diagnostics across multiple temporal scales. *Proceedings of the National Academy of Sciences*, *118*(51). https://doi.org/10.1073/pnas.2023433118

Guglielmi, L., Cappa, F., Avouac, J.-P., Hentry, P., & Elsworth, D. (2015). Seismicity triggered by fluid injection-induced aseismic slip. *Science*, *348*, 1224–1226. https://doi.org/10.1126/science.aab0476

Healy, J. H., Rubey, W. W., Griggs, D. T., & Raleigh, C. B. (1968). The denver earthquakes. *Science*, *161*, 1301–1310. https://doi.org/10.1126/science.161.3848.1301

Heimisson, E. R., Liu, S., Lapusta, N., & Rudnicki, J. (2022). A spectral boundary-integral method for faults and fractures in a poroelastic solid: Simulations of a rate-and-state fault with dilatancy, compaction, and fluid injection. *Journal of Geophysical Research*, *127*, e2022JB024185. https://doi.org/10.1029/2022JB024185

Heimisson, E. R., Rudnicki, J., & Lapusta, N. (2021). Dilatancy and compaction of a rate-and-state fault in a poroelastic medium: Linearized stability analysis. *Journal of Geophysical Research: Solid Earth*, *126*(8), e2021JB022071. https://doi.org/10.1029/2021jb022071

Holland, A. (2011). *Examination of possibly induced seismicity from hydraulic fracturing in the Eola field, Garvin county, Oklahoma*. Oklahoma Geological Survey Oklahoma.

Horton, S. (2012). Disposal of hydrofracking waste fluid by injection into subsurface aquifers triggers earthquake swarm in central Arkansas with potential for damaging earthquake. *Seismological Research Letters*, *83*(2), 250–260. https://doi.org/10.1785/gssrl.83.2.250

Hsieh, P. A., & Bredehoeft, J. D. (1981). A reservoir analysis of the Denver earthquakes. *Journal of Geophysical Research*, *86*(B2), 903–920. https://doi.org/10.1029/jb086ib02p00903

Hubbert, M. K., & Rubey, W. W. (1959). Role of fluid pressure in mechanics of overthrust faulting: 1. Mechanics of fluid-filled porous solids and its application to overthrust faulting. *Geological Society of America Bulletin*, *70*(2), 115–166. https://doi.org/10.1130/0016-7606(1959)70[115:ROFPIM]2.0.CO;2

Keranen, K. M., Savage, H. M., Abers, G. A., & Cochran, E. S. (2013). Potentially induced earthquakes in Oklahoma, USA: Links between wastewater injection and the 2011 Mw 5.7 earthquake sequence. *Geology*, *41*(6), 699–702. https://doi.org/10.1130/g34045.1

Kilgore, B., Beeler, N. M., Lozos, J., & Oglesby, D. (2017). Rock friction under variable normal stress. *Journal of Geophysical Research: Solid Earth*, *122*(9), 7042–7075. https://doi.org/10.1002/2017jb014049

Kim, W.-Y. (2013). Induced seismicity associated with fluid injection into a deep well in Youngstown, Ohio. *Journal of Geophysical Research*, *118*, 3506–3518. https://doi.org/10.1002/jgrb.50247

Lapusta, N., Rice, J. R., Ben-Zion, Y., & Zheng, G. (2000). Elastodynamic analysis for slow tectonic loading with spontaneous rupture episodes on faults with rate- and state-dependent friction. *Journal of Geophysical Research*, *105*, 23765–23789. https://doi.org/10.1029/2000jb900250

Larochelle, S., Lapusta, N., Ampuero, J.-P., & Cappa, F. (2021). Constraining fault friction and stability with fluid-injection field experiments. *Geophysical Research Letters*, *48*(10), e2020GL091188. https://doi.org/10.1029/2020gl091188

Lengliné, O., Boubacar, M., & Schmittbuhl, J. (2017). Seismicity related to the hydraulic stimulation of GRT1, Rittershoffen, France. *Geophysical Journal International*, *208*(3), 1704–1715. https://doi.org/10.1093/gji/ggw490

Linker, M. F., & Dieterich, J. H. (1992). Effects of variable normal stress on rock friction: Observations and constitutive equations. *Journal of Geophysical Research*, *97*, 4923–4940. https://doi.org/10.1029/92jb00017

Liu, Y., & Rice, J. R. (2005). Aseismic slip transients emerge spontaneously in three-dimensional rate and state modeling of subduction earthquake sequences. *Journal of Geophysical Research*, *110*(B8). https://doi.org/10.1029/2004jb003424

Liu, Y., & Rice, J. R. (2007). Spontaneous and triggered aseismic deformation transients in a subduction fault model. *Journal of Geophysical Research*, *112*(B9). https://doi.org/10.1029/2007jb004930

Majer, E. L., Baria, R., Stark, M., Oates, S., Bommer, J., Smith, W., & Asanuma, H. (2007). Induced seismicity associated with enhanced geothermal systems. *Geothermics*, *36*, 185–222. https://doi.org/10.1016/j.geothermics.2007.03.003

Marone, C. (1998). Laboratory-derived friction laws and their application to seismic faulting. *Annual Review of Earth and Planetary Sciences*, *26*(1), 643–696. https://doi.org/10.1146/annurev.earth.26.1.643

Marone, C., Raleigh, C. B., & Scholz, C. H. (1990). Frictional behavior and constitutive modeling modeling of simulated fault gouge. *Journal of Geophysical Research*, *95*, 7007–7025. https://doi.org/10.1029/jb095ib05p07007

Martinez-Garzón, P., Kwiatek, G., Sone, H., Bohnhoff, M., Dresen, G., & Hartline, C. (2014). Spatiotemporal changes, faulting regimes, and source parameters of induced seismicity: A case study from the Geysers geothermal field. *Journal of Geophysical Research*, *120*, 8378–8396. https://doi.org/10.1002/2014JB011385

McClure, M. W., & Horne, R. N. (2011). Investigation of injection-induced seismicity using a coupled fluid flow and rate/state friction model. *Geophysics*, *76*(6), WC181–WC198. https://doi.org/10.1190/geo2011-0064.1

Noël, C., Passelégue, F. X., Giorgetti, C., & Violay, M. (2019). Fault reactivation during fluid pressure oscillations: Transition from stable to unstable slip. *Journal of Geophysical Research*, *124*, 10940–10953. https://doi.org/10.1029/2019JB018517

Noël, C., Pimienta, L., & Violay, M. (2019a). Time-dependent deformations of sandstone during pore fluid pressure oscillations: Implications for natural and induced seismicity. *Journal of Geophysical Research: Solid Earth*, *124*(1), 801–821. https://doi.org/10.1029/2018jb016546

Passelégue, F. X., Brantut, N., & Mitchell, T. M. (2018). Fault reactivation by fluid injection: Controls from stress state and injection rate. *Geophysical Research Letters*, *45*, 12837–12846. https://doi.org/10.1029/2018GL080470

Perfettini, H., Schmittbuhl, J., Rice, J. R., & Cocco, M. (2001). Frictional response induced by time-dependent fluctuations of the normal loading. *Journal of Geophysical Research*, *106*(B7), 13455–13472. https://doi.org/10.1029/2000jb900366

Raleigh, C. B., Healy, J. H., & Bredehoeft, J. D. (1976). An experiment in earthquake control at Rangely, Colorado. *Science*, *91*, 1230–1237. https://doi.org/10.1126/science.191.4233.1230

Ranjith, K., & Rice, J. R. (1999). Stability of quasi-static slip in a single degree of freedom elastic system with rate and state dependent friction. *Journal of the Mechanics and Physics of Solids*, *47*, 1207–1218. https://doi.org/10.1016/s0022-5096(98)00113-6

Rice, J. R. (1993). Spatio-temporal complexity of slip on a fault. *Journal of Geophysical Research*, *98*(B6), 9885–9907. https://doi.org/10.1029/93jb00191

Rice, J. R., Lapusta, N., & Ranjith, K. (2001). Rate and state dependent friction and the stability of sliding between elastically deformable solids. *Journal of the Mechanics and Physics of Solids*, *49*(9), 1865–1898. https://doi.org/10.1016/s0022-5096(01)00042-4

Rice, J. R., & Tse, S. T. (1986). Dynamic motion of a single degree of freedom system following a rate and state dependent friction law. *Journal of Geophysical Research*, *91*(B1), 521–530. https://doi.org/10.1029/jb091ib01p00521

Richardson, E., & Marone, C. (1999). Effects of normal stress vibrations on frictional healing. *Journal of Geophysical Research*, *104*(B12), 28859–28878. https://doi.org/10.1029/1999jb900320

Rubinstein, J. L., Ellsworth, W. L., & McGarr, A. (2012). The 2001-present triggered seismicity sequence in the Raton Basin of southern Colorado/Northern New Mexico. In *Agu fall meeting abstracts*.

Rudnicki, J. W. (2022). Porosity evolution in rate and state friction. *Geophysical Research Letters*, *49*, e2022GL101056. https://doi.org/10.1029/2022GL101056

Rudnicki, J. W., & Chen, C.-H. (1988). Stabilization of rapid frictional slip on a weakening fault by dilatant hardening. *Journal of Geophysical Research*, *93*(B5), 4745–4757. https://doi.org/10.1029/jb093ib05p04745

Rudnicki, J. W., & Yu, T. (2021). Effect of pore pressure oscillations on slip on a fault governed by rate and state friction. In *Proceedings of Biot-Bazant conference*. Retrieved from https://biot-bazant.figshare.com/articles/conference_contribution/Effect_of_pore_pressure_oscillations_on_slip_on_a_fault_governed_by_rate_and_state_friction/14759160

Rudnicki, J. W., & Zhan, Y. (2020). Effect of pressure rate on rate and state frictional slip. *Geophysical Research Letters*, *47*(21), e2020GL089426. https://doi.org/10.1029/2020gl089426

Ruina, A. (1981). *Friction laws and instabilities: A quasistatic analysis of some dry frictional behavior* (unpublished doctoral dissertation). Brown University.

Ruina, A. (1983). Slip instability and state variable friction laws. *Journal of Geophysical Research*, *88*(B12), 10359–10370. https://doi.org/10.1029/jb088ib12p10359

Scuderi, M. M., & Collettini, C. (2016). The role of fluid pressure in induced vs. triggered seismicity: Insights from rock deformation experiments on carbonates. *Nature Scientific Reports*, *6*. https://doi.org/10.1038/srep24852

Scuderi, M. M., & Collettini, C. (2018). Fluid injection and the mechanics of frictional stability of shale-bearing faults. *Journal of Geophysical Research: Solid Earth*, *123*(10), 8364–8384. https://doi.org/10.1029/2018jb016084

Scuderi, M. M., Collettini, C., & Marone, C. (2017). Frictional stability and earthquake triggering during fluid pressure stimulation of an experimental fault. *Earth and Planetary Science Letters*, *477*, 84–96. https://doi.org/10.1016/j.epsl.2017.08.009

Segall, P., & Rice, J. R. (1995). Dilatancy, compaction, and slip instability of a fluid-infiltrated fault. *Journal of Geophysical Research*, *100*(B11), 22155–22171. https://doi.org/10.1029/95jb02403

Sleep, N. H. (1995). Ductile creep, compaction, and rate and state dependent friction within major fault zones. *Journal of Geophysical Research*, *100*(B7), 13065–13080. https://doi.org/10.1029/94jb03340

Wang, L., Kwiatek, G., Rybacki, E., Bohnhoff, M., & Dresen, G. (2020b). Injection-induced seismic moment release and laboratory fault slip: Implications for fluid-induced seismicity. *Geophysical Research Letters*, *47*(22), e2020GL089576. https://doi.org/10.1029/2020gl089576

Wang, L., Kwiatek, G., Rybacki, E., Bonnelye, A., Bohnhoff, M. M., & Dresen, G. (2020). Laboratory study on fluid-induced fault slip behavior: The role of fluid pressurization rate. *Geophysical Research Letters*, *47*(6), e2019GL086627. https://doi.org/10.1029/2019gl086627

Weingarten, M., Ge, S., Godt, J. W., Bekins, B. A., & Rubinstein, J. L. (2015). High-rate injection is associated with the increase in U.S. mid-continent seismicity. *Science*, *348*(6241), 1336–1340. https://doi.org/10.1126/science.aab1345

Yang, Y., & Dunham, E. M. (2021). Effect of porosity and permeability evolution on injection-induced aseismic slip. *Journal of Geophysical Research: Solid Earth*, *126*(7), e2020JB021258. https://doi.org/10.1029/2020jb021258

Yeck, W. L., Weingarten, M., Benz, H. M., McNamara, D. E., Bergman, E. A., Herrmann, R. B., et al. (2016). Far-field pressurization likely caused one of the largest injection induced earthquakes by reactivating a large preexisting basement fault structure. *Geophysical Research Letters*, *43*(19), 10–198. https://doi.org/10.1002/2016gl070861

Zhuang, L., Kim, K., Jung, S., Diaz, M., Min, K.-B., Park, S., et al. (2016). Laboratory study on cyclic hydraulic fracturing of pocheon granite in Korea. In *50th US rock mechanics/geomechanics symposium*.

Zoback, M. D., & Harjes, H.-P. (1997). Injection-induced earthquakes and crustal stress at 9 km depth at the KTB deep drilling site, Germany. *Journal of Geophysical Research*, *102*(B8), 18477–18491. https://doi.org/10.1029/96jb02814